THE UNIVERSITY OF CALGARY

The Distribution of Molecular Nitrogen Ions During a Large Geomagnetic Storm

by

Gregory H. Van Bavel

A THESIS

SUBMITTED TO THE FACULTY OF GRADUATE STUDIES
IN PARTIAL FULFILLMENT OF THE REQUIREMENTS FOR THE
DEGREE OF MASTER OF SCIENCE

DEPARTMENT OF PHYSICS AND ASTRONOMY

CALGARY, ALBERTA

December, 1991

The author has granted an irrevocable non-exclusive licence allowing the National Library of Canada to reproduce, loan, distribute or sell copies of his/her thesis by any means and in any form or format, making this thesis available to interested persons.

The author retains ownership of the copyright in his/her thesis. Neither the thesis nor substantial extracts from it may be printed or otherwise reproduced without his/her permission.

L'auteur a accordé une licence irrévocable et non exclusive permettant à la Bibliothèque nationale du Canada de reproduire, prêter, distribuer ou vendre des copies de sa thèse de quelque manière et sous quelque forme que ce soit pour mettre des exemplaires de cette thèse à la disposition des personnes intéressées.
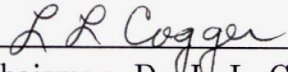
L'auteur conserve la propriété du droit d'auteur qui protège sa thèse. Ni la thèse ni des extraits substantiels de celle-ci ne doivent être imprimés ou autrement reproduits sans son autorisation.
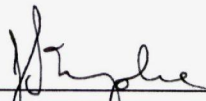
ISBN 0-315-75185-1

Canada

THE UNIVERSITY OF CALGARY
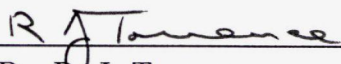
FACULTY OF GRADUATE STUDIES

The undersigned certify that they have read, and recommend to the Faculty of Graduate Studies for acceptance, a thesis entitled, "The Distribution of Molecular Nitrogen Ions During a Large Geomagnetic Storm" submitted by Gregory H. Van Bavel in partial fulfillment of the requirements for the degree of Master of Science.

Chairman, Dr. L. L. Cogger
Department of Physics and Astronomy

Dr. J. S. Murphree
Department of Physics and Astronomy

Dr. R. J. Torrence
Department of Mathematics and Statistics

Date December 23, 1991

Abstract

Through the use of radiative transfer theory for primary scattering with and without extinction, observations by the ISIS 2 satellite of scattered 391.4 nm sunlight by upper atmospheric N_2^+ during the large geomagnetic storm of 18 December, 1971, have produced estimates of the temperature and number density of the N_2^+. Due to instabilities in the spin axis of ISIS 2, and errors inherent in computing the satellite's overall orientation, the ordering of the data is open to correction. The algorithm that uses primary scattering with extinction (PSE) yielded suitable corrections for a series of 5 spins of the satellite; the PSE analysis also provided an effective plasma temperature of the ionized gas of $T = 2420 \pm 70$ K and a number density at 300 km of $n_0 = (2.4 \pm 0.7) \times 10^9 \mathrm{m}^{-3}$. Using these corrections, a second method, which is an adaptation of an commonly used algorithm, could be applied. Systematic errors of hundreds of kilometers in the related altitudes are possible without the corrections to the ordering of the data. The second method used primary scattering with no extinction (PSN), and could only be applied to one spin at a time. However, the PSN approach provided weighted means of $T = 2320 \pm 80$ K and $n_0 = (1.61 \pm 0.03) \times 10^9 \mathrm{m}^{-3}$, where the lower estimate of n_0 can be accounted for by extinction of the 391.4 nm sunlight by upper atmospheric N_2^+.

Acknowledgements

Thanks to Dr. L. L. Cogger for the opportunities and aid provided during the creation of this thesis, and to Dr. J. S. Murphree for the recollection of helpful details some two decades old.

Dedication

To those who maintain scientific research as an opportunity for professional cooperation, rather than an arena for personal conflict.

Contents

List of Tables

List of Figures

Chapter 1

Introduction

1.1 Main Objectives

The main objective of this investigation is to determine the distribution of molecular nitrogen ions (N_2^+) in the upper atmosphere. The actual determination will utilize an indirect method of curve fitting, in which observations of a particular wavelength of sunlight scattered by the N_2^+ and observed by a satellite will be compared to the results of a mathematical model. The model requires the numerical evaluation of a non-trivial integral; hence, a straightforward least-squares best fit analysis is not possible. Secondly, part of the purpose of this task is to identify, or eliminate, physical processes that are involved in controlling the actual distribution of upper atmospheric ions. Having to choose from possibilities that follow from the current understanding of aeronomy, the problem is not to test an accepted model, rather it is to piece together theoretical and empirical fragments that describe a particular feature of the observations. Any conclusions will have to recognize the restrictions that the uncertainties in the data imply. Because of some of the large uncertainties associated with the data, and the absence of accepted models, it is apparent that the fundamental objective is to examine the proposed method of analysis and decide if it is appropriate for the given type of data.

1.2 Overview

1.2.1 Processes of interest

Ionization

As we are to consider the distribution of N_2^+ in the upper atmosphere, then the ionization of neutral diatomic nitrogen seems an appropriate subject to start with in this short overview. The principal mechanism for the production of all ions in the terrestrial ionosphere—where the density of ions reaches its maximum—is *photoionization.* At wavelengths less than ~ 100 nm, incident sunlight induces photoionization of the three major upper atmospheric species: diatomic nitrogen, N_2, diatomic oxygen, O_2, and atomic oxygen, O. Due to the exponential decrease of the density of the neutral atmosphere with altitude and the variation in the direction from which the ionizing sun light is incident over the course of a day, it is not surprising that the ion density distribution is a function of latitude and time of day. Sunlight can also produce ions through *photodissociation,* where larger molecules are destroyed by energetic photons, leaving charged atomic or molecular fragments behind.

Next in importance for the production of ions is *collisional ionization.* Although this source of ions can at times be greater than photoionization, it is sporadic rather than continuous, because it depends upon the channeling of energetic particles into the upper atmosphere. The conditions necessary for guiding the ionizing particles into the ionosphere coincide with the presence of aurora; however, the link is not absolute. Electrons, e^-, are the most important particle providing for collisional ionization, as they are the lightest and most numerous among the possibilities, which include protons, ions, and neutral particles. *Chemical reactions* are also an important

source of ions. The numerous reactions that affect the concentrations of all the ionic species are dependent on a variety of conditions; in fact, under some conditions a chemical reaction, or a series thereof, will be initiated such that a sink for some species of ions will be in effect. Deciding when the local chemistry of the upper atmosphere will provide for a source or a sink of an ion of interest is an area of active research.

Resonant Scattering

Given the presence of N_2^+, then the next physical process of interest to us is that of *resonant scattering*. The scattering of light can be accomplished by many known mechanisms; in any given instance, it is the frequency of radiation and the physical characteristics of the matter that govern the actual interactions between radiation and matter. It is the case where the radiation is absorbed and then emitted at the *same* frequency that distinguishes resonant scattering from other forms. The specific case of interest is the aborption of a 391.4 nm photon by N_2^+ in its ground energy state and the subsequent return of the ion to the ground state after a 391.4 nm photon is emitted in some direction, not necessarily in the direction of the incident photon. If the direction of the scattered photon is independent of the direction of the incident photon, then the scattering is called isotropic; this property is not found in real atmospheres in most types of scattering, including resonant scattering.

Radiative Transfer

The third major topic pertaining to the physics of our problem is *radiative transfer*. This theory constructs a systematic description of the large scale, or average, behavior of radiation as it passes through a non empty medium. Each particle in

the medium presents a certain amount of target area to the incident light, and the fraction of light that passes through some distance in the medium is proportional to the fraction of the total area of the scattering material to the area over which the beam of light extends. This idea of radiation continually undergoing losses as it passes through matter gives rise to the notion of *optical depth*—the larger the optical depth a particular beam of light has passed, the smaller the fraction of the original light will be left.

Within the scope of radiative transfer theory, there is a useful recipe for modeling the satellite observations of 391.4 nm photons by N_2^+ called *primary scattering*. This model assumes that along any line of sight of an observer, the majority of photons observed are due to a single scattering event. This assumption is valid in the context of terrestrial N_2^+ scattering sunlight in the upper atmosphere because the incident sunlight at the wavelength of interest is so much more intense than that which is scattered out of the incident beam. Going too low into the atmosphere would be stepping outside the bounds of the assumption, since the multiple scattering of a photon becomes more probable in the denser medium, and other particles colliding with an excited N_2^+ can steal the energy away in a collision before a scattered photon is emitted. Primary scattering considers only one scattering event for each incident photon—either the photon enters the observer's field of view and is noted by the observer, or it is lost. Having discussed briefly some important physical concepts related to the production of the observed quantities, which are photons, we can now proceed to the satellite that serves as the detector.

1.2.2 Observations

The ISIS 2 satellite returned 391.4 nm intensity measurements, which were gathered with the auroral scanning photometer (ASP), to ground based receiving stations. The nearly circular orbit with an inclination of about 90 degrees ensured that the ISIS 2 satellite had the potential to make auroral observations as it passed over the poles of the earth. From a vantage point some 1400 km in altitude, the spinning satellite would direct the ASP through a full 360 degree scan. At best, one third of the time the ASP was pointed at the earth or into the atmosphere above its limbs, which is what we shall be interested in; at worst, no useful measurements could be made. The direction of the line of sight of a particular observation of the 391.4 nm intensity was not a part of the data transmission, rather, the universal time of observation was the distinguishing tag on each observation.

The actual line of sight would be determined from other data, namely 557.7 nm (the auroral green line) intensity measurements and an assumed height of the 557.7 nm limb. Fitting the data to the expected limb observations provided the ASP line of sight as a function of time, and a "best fit" spin axis orientation. Any modeling of the data would suffer from a poor determination of either the ASP line of sight , or the ISIS 2 spin axis. Much effort has gone into refining this technique; however, the uncertainties that it introduces cannot be dismissed.

1.2.3 Data Analysis

The data analysis was not as straight forward as one would optimistically anticipate. Although the results appear reasonable, the scope of the analysis had to be greatly reduced because of problems with the ordering of the data. The aim of including

both morning and evening side limb observations had to eventually be abandoned. The problem is apparently related to the stability of the satellite; there is evidence, discussed in [46], that the spin axis of the satellite wobbles such that the spin axis vector is not constant as required. Even worse, there is also good evidence that the spin axis does not always coincide with the axis of symmetry. Thus, modeling the observations becomes a matter of discovering a segment of data that provides for reasonable agreement. The lengthy sifting of the data is the major practical flaw of the analysis, because the more data one discards, the greater the probability of skewing the results one way or another.

1.2.4 Results

The temperature T and number density n_0 results were found to be in reasonable agreement with previous observations made by other means. However, the correction factor found for the calibration of the auroral scanning photometer is a reduction to about 37% of its original value. Thus, it would seem that if the model is correct, the cumulative error in estimating the various parameters related to the conversion of the photometer's observations to a column density implies a reduction of about two thirds in the given calibration. This result is good grounds for being skeptical about the accuracy of the rest of the results—one usually expects the calibration to be out by a factor of 2, at most, either way. We will attempt to assuage our doubts by further discussion and examination of other related factors, such as some assumptions used in the construction of the model.

Chapter 2

ISIS 2 and the Auroral Scanning Photometer

2.1 The ISIS 2 Satellite

The ISIS acronym follows from the International Satellites for Ionospheric Studies
project of which the ISIS 2 satellite is the fourth to be launched. The launch occurred
on the first day of April in 1971. While most satellite photometers at the time were
fixed in one direction and would scan the earth only as a result of the orbital motion
of the satellite, the dual wavelength photometer on the ISIS 2 satellite was to use
the spin of the satellite itself to add a second mode of scanning, and method of
photometer image dissection to add a third. In this way, the joint Canadian and U.
S. experiment was to produce data that would allow greater detail in the study of
auroral distributions and morphology.

The ISIS 2 orbit was nearly circular with a mean orbital altitude a little less than
1400 km. The inclination of the orbit was about 88 degrees, which means that it
would pass over both of the earth's poles in the course of an orbit; hence, the orbit
is referred to as a polar orbit. The orbital period is a nearly two hours, and the spin
period about 18 seconds. Thus, there was the potential of revisiting an interesting
auroral event at either pole every two hours.

Solar cells on the outer faces of the satellite were the main sources of power for
ISIS 2. The external cells charged internal nickel-cadmium batteries, which could
deliver some 125 W of power to the onboard experiments and telemetry electron-
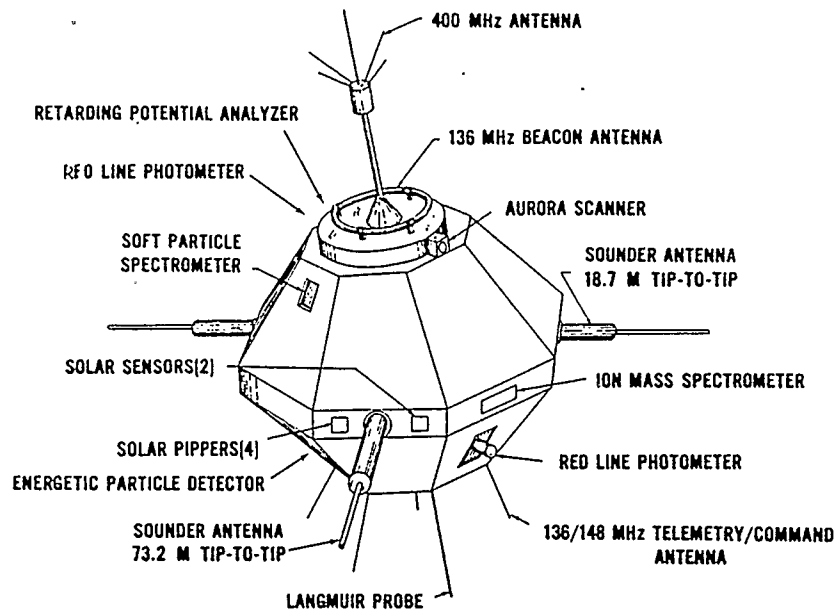
Figure 2.1: ISIS 2 and its instrumentation

ics. Moreover, the electrical system also provides the attitude control by setting up magnetic fields in the satellite that interact with the terrestrial magnetic field to provide a means of guiding the direction in which the spin axis points. There were two extremes that characterized the relative configuration of the spin axis and orbital plane; the first was the orbit aligned mode, where the spin axis was in the orbital plane and the photometer would scan perpendicular to the orbital plane; the second was the cartwheel mode where the spin axis was perpendicular to the orbital plane and the photometer scans were restricted to the same plane. In the former mode, each scan covered new territory as the satellite moves in its orbit, whereas in the latter mode each scan covered the same territory.

The experiments on board the ISIS 2 satellite, shown in Figure 2.1, are:

- Swept frequency sounder

- Fixed frequency sounder

- Very low frequency receiver

- Cosmic noise experiment

- 136/137 beacon experiment

- Energetic particle detector

- Ion mass spectrometer

- Cylindrical electrostatic probe

- Ion temperature measurements

- Red line photometer

- Auroral scanning photometer (ASP)

A good brief description of the ISIS 2 instruments is given in [46], and a more detailed discussion can be found in [15].

2.2   The Auroral Scanning Photometer

The ASP has two viewing directions separated by approximately 180 degrees, each of which corresponds to a different wavelength of interest. In one direction there is a 557.7 nm filter with a full width at half maximum (FWHM) of 1.8 nm, in the other direction there is a 391.4 nm filter with a FWHM of 2.6 nm. By directing incoming light with lenses and mirrors, it is possible to have the two viewing directions share

a common photo cathode. The data from the two viewing directions did not, for the most part interfere with each other, as one line of sight would be off earth; however, the off earth field of view could contain stars, which would produce noise in the data, and if either the moon or sun were in the off earth field of view the data would not be of use.

Through the use of an image dissector, the common cathode was divided into 13 individual elements, roughly analogous to solid state pixels. The data from only one element was gathered at any one time. By passing from one element to the next, the field of view was effectively moved parallel to the spin axis, which is in addition to the spinning motion that would move the field of view perpendicular to the spin axis. This method of scanning is shown in Figure 2.2. Each element had a nearly square field of view that was some 0.4 by 0.4 degrees in extent, which corresponds to about 28 km at the point where the line of sight is tangent the earth at a height of 300 km—this altitude of 300 km is also referred to as the *tangential height* of the line of sight. The lower end of the dynamic ranges of either of the wavelengths were set to correspond to the lowest airglow or auroral intensities expected to be of interest as suggested by previous ground based observations.

The problem of keeping direct sunlight out of the ASP was to be solved through the use of a two stage baffle system. The outer baffle was to provide protection when the angle Θ between the line of sight and the incident sunlight was greater than $\sim 40°$, and the inner baffle was to act as a back up for $\Theta < 17°$. Regardless of the minimum value of Θ for any scan, a fail-safe detector protects the photomultiplier from destructive exposures. The black coating on the inner baffles still produced 2.8 % total hemispheric reflectance; hence, contamination continued to be a problem
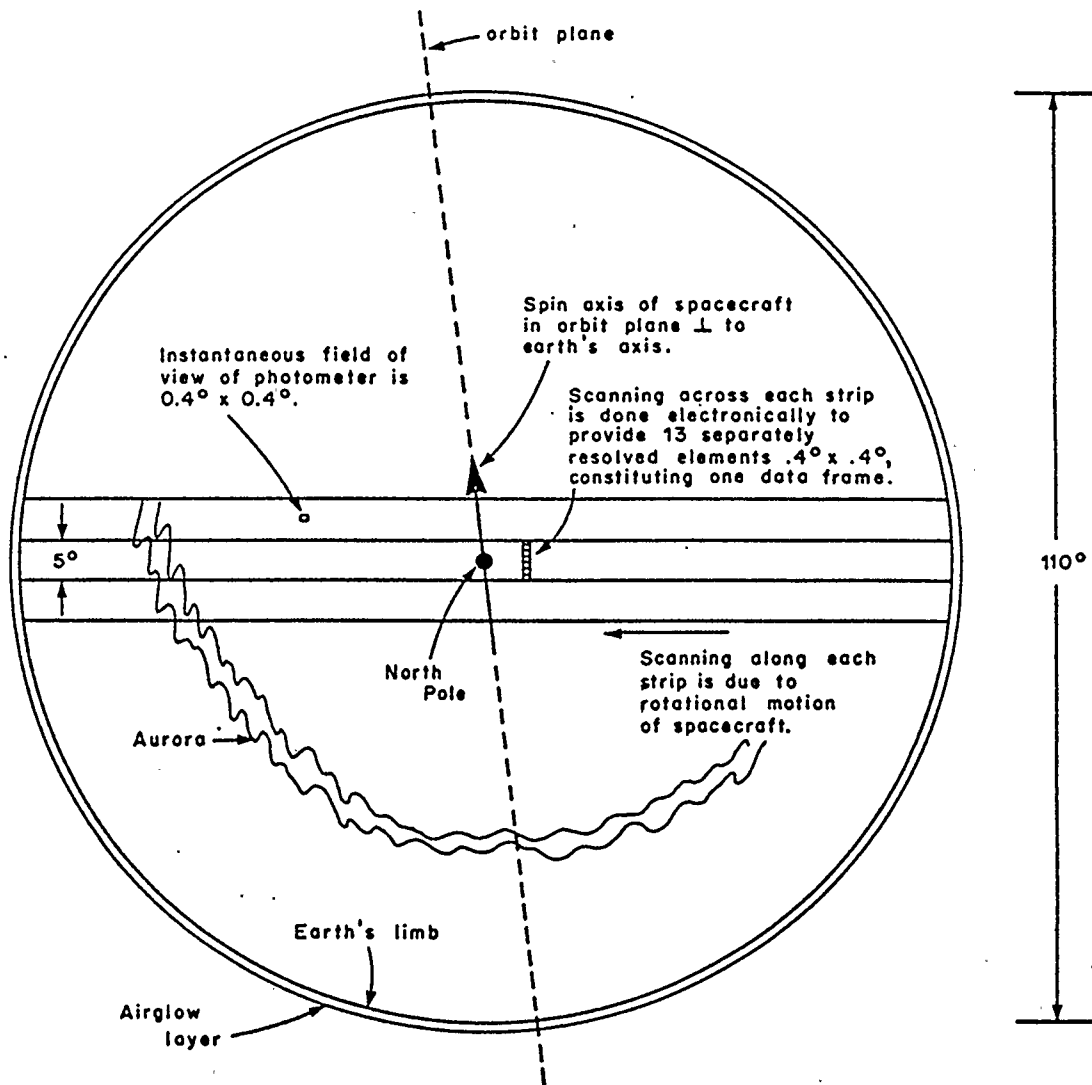
Figure 2.2: The scanning pattern of the auroral scanning photometer, where the 5° strips are scanned during successive rotations due to the orbital motion of the satellite.

with direct sunlight reflected off the baffles mixed with the desired scattered light. Baffle contamination was strong for the cases where $\Theta < 60°$, and the noise was worse when the angle Φ between the spin axis and the incident sunlight was such that $\Phi < 120°$. It is unfortunate that large amounts of data suffer from the problem of baffle scattering, and attempts to find a useful correction for the noise have failed, simply because of the dependence of the contamination on both Θ and Φ.

The other sources of uncertainty in the ASP observations are directly related to the photometer itself. For a given standard light source, the 13 elements provided by the image dissector did not respond in a uniform manner. Thus, correction factors must be applied to the data according to the element from which it came. A common correction that must be made to all counting detectors such as the ASP is a dead time correction. These become important when high intensities are being observed, because the probability of a photon striking the photocathode while the effects of the previous photon are still present becomes greater. A dependence of the dead time correction on the intensity was also found to be a feature of the ASP. The signal that the ASP produces even when no light hits the cathode is the dark current, which was found to be correlated with the temperature measured by a probe on the ISIS 2 satellite. However, both the temperature and the dark current vary with Φ, which is the angle between the spin axis and the incident sunlight.

Data from the ASP was processed on board the satellite at a bit rate of 4410 Hz. The information from the 13 elements was gathered one at a time at a rate of 630 Hz, an extra "element" was included for the purposes of signal processing syncronization. The 14 elements, 13 of which were ASP data, are referred to as a data *frame* and were processed at a rate of 45 Hz. An inertial or relative indication of the direction

of the ASP line of sight was not a part of the data output from the satellite, nor was the ISIS spin axis. Both of these important pieces of information result from the fit of the 557.7 nm data to an assumed altitude of the actual 557.7 nm limb. The precision of our knowledge of the attitude of the satellite is limited by both the precision of the observed data and its organization, and an assumption of a fixed ionospheric feature in a system that is highly dynamic. The uncertainties that this introduces into the data are far from negligible and must be considered before any conclusions drawn from the data are entertained.

2.3   Earlier Observations

The observations of airglow began with the twentieth century. The earliest investigations were interested in establishing where the airglow originated. It was not a matter of where in the terrestrial atmosphere the light originated, rather the possibilities included faint stars and zodiacal light. The theory describing the airglow source region that is now generally accepted was proposed by Sidney Chapman in 1931. This successful theory provides for other atmospheric emissions of light, such as aurorae, through the presence of an ionosphere, where photons are emitted due to ever present activity that includes ionization, recombination, and the reduction of excited particles to their ground state.

Having established where the airglow originated, the next step was to identify the particles involved. This required both the detailed laboratory results and the theoretical studies of spectroscopy. The band structure of molecular spectroscopy, which will be discussed further below, introduced an obvious indicator of the presence

of molecules in airglow spectra; however, the overlapping of the bands of several species also complicated the process of identifying an individual molecule. Hence, a prominent feature in the observed spectrum that could be associated with a specific molecule was valuable. This feature is present at 319.4 nm in the band spectrum emitted by N_2^+, and for this reason molecular nitrogen ions were the first species identified and studied in the early years of twilight airglow investigations.

A full review of the early airglow work is given in [35], where the first attempts to combine new instruments and theory in the study of the upper atmospheric composition were discussed. In addition, mention is made of the difficulties of calibrating detectors, and the unsatisfying data reduction techniques that were employed. Some twenty years later, these same problems still continue to bedevil airglow (and auroral) investigations that include ground, rocket, and satellite based detectors.

Due to the work of A. L. Broadfoot and others, in [14] and [12], an important parameter associated with the emissions of N_2^+ called g, the photon scattering coefficient, was established. A table of g values for commonly observed upper atmospheric species is given in [17], among others. It was with the fixing of g, although somewhat uncertain, that allowed for the possibilty of quantitative investigations of upper atmospheric N_2^+ in absolute, rather than relative, terms. This type of investigation was performed on ISIS 2 data in [73], which serves as the prototype for the analysis to follow.

However, it was eventually conceded that the value of g was not the greatest source of error in the analysis of airglow observations, rather it was the neglect of radiative transfer effects. Our attempt to remove this obstacle is discussed next.

Chapter 3

Scattering of Sunlight by N_2^+

3.1 Fundamentals

3.1.1 Electrodynamic Basis for Scattering

The following discussion is adapted from [38], where the consideration of radiative effects on the motion of a charged particle led to the definition of a *characteristic* time τ, which is a parameter estimated with the use of the nonrelativistic Larmor formula for the power radiated by an accelerated particle

$$\tau = \frac{2}{3}\frac{e^2}{mc^3} \tag{3.1}$$

where e is the elementary charge, m is the particle's mass, and c is the speed of light. If the acceleration of a charge occurs over some time t, where $t \gg \tau$, then radiative effects are not important; when $t \sim \tau$, then the emission of radiation by the accelerated particle will greatly affect the particle's motion. The Abraham-Lorentz equation of motion is an approximate and time-averaged description of the motion of a charged particle when $t \sim \tau$. If a radiative reaction force is included in the Newton equation of motion, and the work done by the reaction force is related to the power radiated according to the Larmor formula, then the Abraham-Lorentz equation of motion is found to be

$$m\frac{d^2\mathbf{x}}{dt^2} = \mathbf{F} + m\tau\frac{d^3\mathbf{x}}{dt^3} \tag{3.2}$$

15

where **F** is the external force on the particle, and the second term on the right hand side of (3.2) is the radiative reaction force.

The limitations of the Abraham-Lorentz model are many; however, the ease with which it provides rudimentary physical insight into the problem of radiation scattering leads us to neglect the deficiencies. By adding a term, $m\omega_0^2\mathbf{x}$, to mathematically describe a restoring force, then (3.2) can be modified such that it now portrays, to first order, the scattering of radiation by bound charges. Of course, the external force **F** is now due to the incident radiation

$$\mathbf{F} = e\mathbf{p}_i E_0 e^{-j\omega t} \tag{3.3}$$

where $\mathbf{p}_i$ is the incident polarization vector, E_0 is the electric field at the center of force, and ω is the frequency of the incident radiation. In addition, a resistive term, $m\Gamma'\frac{d\mathbf{x}}{dt}$, which is first order in the velocity, can be included in order to allow for dissipative processes, with Γ' being the damping constant. Adding the restoring and resistive terms to the left hand side of (3.2), and then substituting (3.3) for F yields

$$-\tau\frac{d^3\mathbf{x}}{dt^3} + \frac{d^2\mathbf{x}}{dt^2} + \Gamma'\frac{d\mathbf{x}}{dt} + \omega_0^2\mathbf{x} = \frac{e}{m}\mathbf{p}_i E_0 e^{-j\omega t}$$

This linear third order differential equation has the following steady-state solution

$$\mathbf{x} = \frac{e}{m}\frac{E_0 e^{-j\omega t}}{\omega_0^2 - \omega^2 - j\omega\Gamma_t}\mathbf{p}_i \tag{3.4}$$

where Γ_t is

$$\Gamma_t(\omega) = \Gamma' + \left(\frac{\omega}{\omega_0}\right)^2 \Gamma$$

and $\Gamma = \omega_0^2 \tau$ is the *radiative decay constant.*

The Lienart-Wiechert radiation electric field due to the nonrelativistic accelera-
tion of charges is, at a point distant from the bound charges,

$$\mathbf{E} = \frac{e}{c^2}\frac{1}{r}[\mathbf{n} \times (\mathbf{n} \times \ddot{\mathbf{x}})]$$

where $\mathbf{n}$ is a unit vector indicating the direction of the observer relative to the bound
charges, r is the distance from the charges to the observer, and $\ddot{\mathbf{x}}$ is the second total
time derivative of $\mathbf{x}$ given by (3.4). In order to find the magnitude of $\mathbf{E}$ for some
scattering polarization $\mathbf{p}_s$, we first form the inner product of the field and polarization
vectors with one of the two in its complex conjugate form

$$\mathbf{p}_s^* \cdot \mathbf{E} = \frac{e^2}{mc^2}\omega^2 \frac{E_0 e^{-j\omega t}}{\omega_0^2 - \omega^2 - j\omega\Gamma_t}\left(\frac{\mathbf{p}_s^* \cdot \mathbf{p}_i}{r}\right) \qquad (3.5)$$

With σ denoting cross sectional area per unit frequency interval and Ω denoting the
solid angle about the scatterer, then by the definition of differential scattering cross
section, which is

$$\frac{d\sigma}{d\Omega} = \left|\frac{r\mathbf{p}_s^* \cdot \mathbf{E}}{E_0}\right|^2$$

such that when it is combined with (3.5) the result is

$$\frac{d\sigma}{d\Omega}(\omega, \mathbf{p}_s) = \left(\frac{e^2}{mc^2}\right)^2 |\mathbf{p}_s^* \cdot \mathbf{p}_i|^2 \left[\frac{\omega^4}{(\omega_0^2 - \omega^2)^2 + \omega^2\Gamma_t^2}\right] \qquad (3.6)$$

The Rayliegh law of scattering corresponds to the condition $\omega \ll \omega_0$ placed on (3.6), and the differential cross section is

$$\frac{d\sigma_{Ry}}{d\Omega}(\omega, \mathbf{p}_s) = \left(\frac{e^2}{mc^2}\right)^2 |\mathbf{p}_s^* \cdot \mathbf{p}_i|^2 \left(\frac{\omega}{\omega_0}\right)^4$$

where the required fourth power dependence on frequency is present. At the other extreme, $\omega \gg \omega_0$, the Thomson differential cross section is obtained

$$\frac{d\sigma_T}{d\Omega}(\omega, \mathbf{p}_s) = \left(\frac{e^2}{mc^2}\right)^2 |\mathbf{p}_s^* \cdot \mathbf{p}_i|^2 (1 + \omega\tau)^{-1}$$

however, the free particle value is subject to the radiation damping correction term $(1 + \omega\tau)^{-1}$, which in the classical domain is unity because $\omega \ll 1/\tau$. Thus, at lower frequencies, the scattering of radiation follows the Rayleigh law, while at higher frequencies, Thomson scattering is important. It is between these two types of scattering that resonant scattering is found. When $\omega \approx \omega_0$, then (3.6) provides the following approximation

$$\frac{d\sigma_R}{d\Omega}(\omega, \mathbf{p}_s) = \frac{9}{16}\left(\frac{c}{\omega_0}\right)^2 \frac{\Gamma^2}{(\omega - \omega_0)^2 + (\Gamma_t/2)^2} |\mathbf{p}_s^* \cdot \mathbf{p}_i|^2 \tag{3.7}$$

If (3.7) is integrated over all solid angles and scattering polarizations, the total scattering cross section per unit frequency is

$$\sigma_R(\omega) = \frac{3\pi}{2}\left(\frac{c}{\omega_0}\right)^2 \frac{\Gamma^2}{(\omega - \omega_0)^2 + (\Gamma_t/2)^2} \tag{3.8}$$

The relative scattering cross section, $\sigma_R(\omega)/\sigma_R(\omega_0)$, versus the relative frequency,
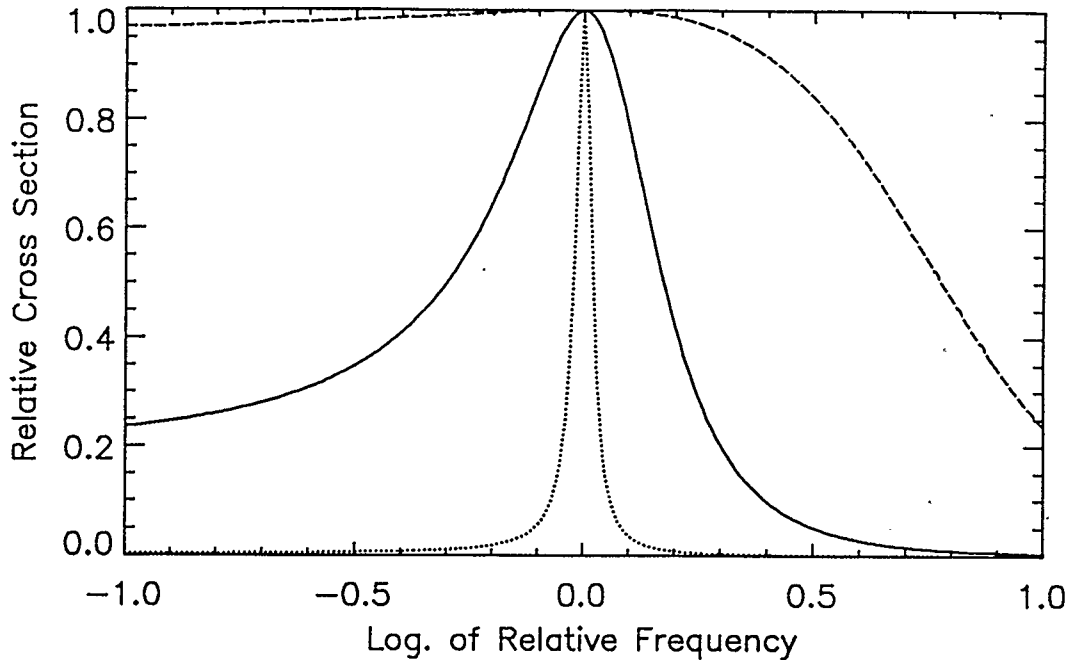
Figure 3.1: The relative total scattering cross section for relative frequencies near resonance. The solid line corresponds to $\Gamma'/\omega_0 = 1$, the dotted line $\Gamma'/\omega_0 = 0.1$ and the dashed line $\Gamma'/\omega_0 = 10$.

$\log_{10}(\omega/\omega_0)$, is shown for (3.8) in Figure 3.1 with three values of of the damping constant Γ'—note that in the classical domain, the radiative decay constant $\Gamma = \omega_0^2 \tau$ can be neglected.

Quantum mechanics provides for a similar expression for σ_R; however, the angular momenta of the ground and excited states enter into the solution. That is, if the right hand side of (3.8) is multiplied by the following factor, then it will agree with the result obtained with quantum mechanics

$$\frac{2}{3}\left[\frac{2J_i + 1}{2(2J_0 + 1)}\right]$$

where J_0 is the angular momentum number of the ground state, and J_i is the angular

momentum of the ith excited state. The classical result corresponds to $J_i = 1$ and $J_0 = 0$.

From the above mathematical sketch, it can be seen that the resonant scattering of radiation is a part of a continuum of interactions between radiation and matter, which has been modeled similar to a damped oscillator. In addition to resonant scattering not being an isolated feature for a particular mode of oscillation, there are further complications due to the fact that there are many different modes in which a molecule might oscillate and store the excitation energy. Let us move on now to consider the notation by which the different spectroscopic features are labeled such that a common identification of the different modes can be made.

3.1.2 Molecular Spectroscopy

A quantum mechanical analysis of the structure of a molecule is a search for "good" quantum numbers that correspond, in some regular way, to the observed behavior of the molecule—especially as far as spectroscopic features are concerned. The quantity of useful quantum numbers are limited by the symmetry present in the molecule; the structure of the molecule also limits the extent to which a meaningful, or useful, mathematical model can be constructed to describe the molecule. Diatomic molecules, such as N_2^+ which is of direct interest, offer the fewest barriers to a theoretical analysis. If the two atoms in the molecule differ, the detail to which the state of the molecule can be specified is immediately reduced. Polyatomic molecules that have little or no symmetry defy anything other than a statistical analysis.

The energy states associated with the electronic structure of a molecule show the greatest separation (in energy) between adjacent states. Diatomic molecules can

be assigned a good orbital momentum number because of the symmetry about the internuclear axis. However, since the force on the orbiting electrons is not central, the orbital momentum is not a conserved quantity. The projection along the internuclear axis of the total orbital angular momentum provides the quantum number Λ. It is the rotational symmetry about the internuclear axis that Λ indicates. In an analogous manner to S, P, D, and F of atomic spectroscopic notation, capital Greek letters correspond to the integer values of Λ: $\Sigma \Rightarrow (\Lambda = 0)$, $\Pi \Rightarrow (\Lambda = 1)$, $\Delta \Rightarrow (\Lambda = 2)$, *etc.*

Reflection symmetries allow for further description of the state of a molecule. Homonuclear molecules, like N_2^+, are characterized by reflection symmetry about a plane which is perpendicular to the internuclear axis, and which bisects it. The term *gerade*, meaning even and abbreviated to g, is applied in the case where the wave function does not change sign when reflected across that plane; similarly, the term *ungerade*, meaning odd and abbreviated to u, is applied in the case where the wave function does change sign upon reflection. For the plane that contains the internuclear axis, symmetry exists only for the $\Lambda = 0$, or Σ, state because this state is characterized by cylindrical symmetry about the internuclear axis, whereas for $\Lambda > 0$ no similarly useful feature is present. If the wave function does not change sign about this second plane, then the state is labeled with a $+$, and the opposite behavior is labeled with a $-$.

The total spin of the electrons, which is denoted with a Σ and is not to be confused with the usage discussed above where $\Sigma \Rightarrow (\Lambda = 0)$, is a second useful quantum number related to the specification of the electronic state of a molecule. The total electron angular momentum Ω, is conserved and is given by $\Omega = |\Sigma + \Lambda|$.

The standard notation that displays the above infromation is

$$\Upsilon^{2\Sigma+1}\Lambda^{+\,\text{or}\,-}_{u\,\text{or}\,g}$$

where Υ symbolizes a capital Roman letter that is used to indicate the electronic energy state: and X denotes the ground state, while letters near the beginning of the alphabet, such as A, B, C, *etc*, are understood to be excited states. Unfortunately, there is no direct correspondence between the relative energies of each state and the alphabetical order of the letters labeling them. The transition of interest, which gives rise to the resonant scattering of 391.4 nm sunlight by N_2^+, is

$$B^2\Sigma_u^+ \quad \longrightarrow \quad X^2\Sigma_g^+$$
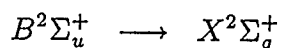
In contrast to atoms, molecules have ways other than the variation of electron configurations to store energy. First, molecules can vibrate along the axes connecting nuclei. Diatomic molecules can be approximated by a simple harmonic oscillator for vibrations of relatively low energy. The energy E_v is quantized according to the following quantum mechanical result

$$E_v(n) = h\nu\left(n + \frac{1}{2}\right)$$

where h is Planck's constant, ν is the frequency of oscillation, and n is the quantum number. For larger n, higher order terms must be included if the anharmonic character of the larger vibrations is to be well described. A second way that molecules can store energy, which atoms cannot, is through rotation of the extended molecular

structure about some axis. For a diatomic molecule, the discrete energy levels E_r are given by

$$E_r(J) = \frac{J(J+1)}{2I_v}\hbar^2$$

where J is the rotational number, I_v is the moment of inertia that depends upon the distance between the nuclei and so is dependent upon the vibrational state of the molecule, and $\hbar$ is Planck's constant divided by 2π. If we associate E_e with the energy related to changes in the electronic structure of the molecule, then when the relative magnitudes of vibrational energies E_v and rotational energies E_r are compared with E_e the following order is established

$$E_e \gg E_v \gg E_r$$

This ordering accounts for the observed spectroscopic band structure associated with molecules. The distance (in energy) between bands is determined by E_e, the extent of a band is determined by E_v, and the spacing of lines featured within a band is determined by E_r.

For diatomic molecules, the dipole selection rules for allowed transitions are

$$\Delta\Sigma = 0$$

$$\Delta\Lambda = 0, \pm 1$$

$$\Delta\Omega = 0, \pm 1, \text{ (no } 0 \rightarrow 0)$$

In addition, for homonuclear diatomic molecules, we have

$$u \rightarrow g \ \text{ or } \ g \rightarrow u$$

$$+ \rightarrow + \ \text{ or } \ - \rightarrow -$$

However, all of the above selection rules are subject to the Frank-Condon principle: the internuclear distance must be nearly equal before and after the transition. That is, if the vibrational/rotational states of two different electronic states do not provide for an overlap in the internuclear separation, then the probability of the transition is greatly reduced.

3.2 Radiative Transfer

3.2.1 General Equations

The problem of primary scattering has been developed using radiative transfer theory. Before discussing the particular case of primary scattering of 3914Å sunlight by N_2^+, the relevant general concepts of radiative transfer are to be considered. For any geometry, the transfer equation can be written for some point r in space

$$\Omega \cdot \nabla I(\mathbf{r}, \Omega) = -\sigma_e(\mathbf{r})[I(\mathbf{r}, \Omega) - J(\mathbf{r}, \Omega)] \tag{3.9}$$

where Ω denotes the direction of propagation of the radiation, I is the radiance or specific intensity, σ_e is the volume extinction coefficient, and J is the source function for the radiation field. There are two radiative processes that contribute to σ_e: they

are absorption and scattering of the radiation by material in the medium. That is, σ_e is given by

$$\sigma_e(\mathbf{r}) = \sigma_s(\mathbf{r}) + \sigma_a(\mathbf{r}) \tag{3.10}$$

with σ_s being the volume scattering coefficient, and σ_a being the volume absorption coefficient.

The optical depth (optical length), τ of a medium along a line $\mathbf{L}$ is defined as

$$\tau = \int_a^b \sigma_e(\mathbf{r}(l))\, dl \tag{3.11}$$

where l is a parameter along the line of integration, which is initially a and finally b. Thus, (3.11) gives the optical depth that the radiation must traverse between points $\mathbf{r}(a)$ and $\mathbf{r}(b)$ on $\mathbf{L}$. If the extinction cross section, α_e, of some matter of number density $n(\mathbf{r})$ is independent of $\mathbf{r}$ then

$$\sigma_e(\mathbf{r}) = \alpha_e n(\mathbf{r}) \tag{3.12}$$

By substituting (3.12) into (3.11), it is apparent that when α_e is given, then the calculation of τ is dependent upon knowledge of $n(\mathbf{r})$

$$\tau = \alpha_e \int_a^b n(\mathbf{r}(l))\, dl \tag{3.13}$$

It is (3.13) that will be of interest when a particular form of (3.9) is applied to the problem below.

The phase function, p, for radiation of frequency ν provides the probability that

radiation propagating in direction Ω_0 will be scattered at point $\mathbf{r}$ into the direction Ω_1. The phase function is normalized over all possible scattering angles

$$\frac{1}{4\pi} \oint p(\mathbf{r}, \Omega_0, \Omega_1)\, d\Omega_1 = 1 \tag{3.14}$$

If an angle Θ is defined as

$$\cos(\Theta) = \Omega_0 \cdot \Omega_1 \tag{3.15}$$

and p is dependent only upon Θ and $\mathbf{r}$, then (3.14) reduces to

$$\frac{1}{2} \int_0^\pi p(\mathbf{r}, \Theta)\, \sin(\Theta)\, d\Theta = 1 \tag{3.16}$$

Isotropic scattering is equivalent to

$$p(\mathbf{r}, \Theta) = 1 \tag{3.17}$$

which is a property never found in real atmospheres. However, unless very precise measurements are being considered, then (3.17) is a useful simplification.

Now it is possible to make the most general statement about the source function, $J(\mathbf{r}, \Omega)$,

$$J(\mathbf{r}, \Omega) = \frac{\sigma_s}{4\pi\sigma_e} \oint p(\mathbf{r}, \Omega_0, \Omega) I(\mathbf{r}, \Omega_0)\, d\Omega_0 + J_l(\mathbf{r}, \Omega) \tag{3.18}$$

where $J_l(\mathbf{r}, \Omega)$ is due to local internal and/or external sources of radiation, and the definition of net flux, F, through a surface with a normal vector $\mathbf{n}$ is

$$F = \frac{1}{\pi} \oint I(\mathbf{r}, \Omega)\, \Omega \cdot \mathbf{n}\, d\Omega \tag{3.19}$$

3.2.2 Primary Scattering

Briefly stated, the conditions for primary scattering are

$$\sigma_a \ll \sigma_s \tag{3.20}$$

$$\tau < 1 \tag{3.21}$$

$$I_1(\mathbf{r}, \Omega) \gg I_k(\mathbf{r}, \Omega); \quad k = 2, 3, 4, \ldots \tag{3.22}$$

The first condition, (3.20), states that there is little absorption of the radiation of interest; it is mainly scattering that contributes to the extinction, $\sigma_e \simeq \sigma_s$. The second statement, (3.21), implys that the medium is, by definition, optically thin to the radiation; in the terminology of transport theory, the observer is within one mean free path of the point at which the radiation of interest was scattered. Condition (3.22) holds that the radiance due to one scattering event, which, by definition, is radiance due to primary scattering, is always far greater than the radiance that has been subject to secondary, tertiary, etc., scattering. In addition, for the sake of completeness it should be stated that along the direction of propagation, Ω_0, of the incident radiation, I_0, it is the case that

$$I_0(\mathbf{r}, \Omega_0) \gg I_1(\mathbf{r}, \Omega_0) \tag{3.23}$$

Obviously, observations in the direction of $-\Omega_0$ can not be included in observations of radiation subject to primary scattering.

Under conditions (3.20), (3.21), and (3.22), the equation of transfer (3.9) along

the direction of propagation of the scattered radiation, I_1, becomes

$$\frac{dI_1}{ds_1} = \alpha_e n(\mathbf{r}_1(s_1))[I_1(s_1) - J_1(s_1)] \tag{3.24}$$

where (3.12) was substituted into (3.9), α_e is the extinction cross section of the scattering material, which is present at a number density $n(s_1)$, and s_1 is a parameter along the line of sight of the observer, such that any point, $\mathbf{r}_1$, along the line of sight is given by

$$\mathbf{r}_1(s_1) = \mathbf{P} - s_1\mathbf{\Omega}_1, \quad s_1 \geq 0 \tag{3.25}$$

where $\mathbf{P}$ is the location of the observer, whose line of sight is in the direction $-\mathbf{\Omega}_1$. Note that the chain rule and (3.25) provide

$$\frac{dI_1}{ds_1} = \nabla I_1 \cdot \frac{d\mathbf{r}_1}{ds_1} = \nabla I_1 \cdot (-\mathbf{\Omega}_1) = -\mathbf{\Omega}_1 \cdot \nabla I_1$$

Similarly, in the direction of propagation, $\mathbf{\Omega}_0$, of the incident radiation, I_0,

$$\frac{dI_0}{ds_0} = \alpha_e n(s_0, s_1) I_0(s_0, s_1) \tag{3.26}$$

where $J_0 = 0$ as (3.23) implies, and s_0 is a parameter along $\mathbf{\Omega}_0$ to $\mathbf{r}_1(s_1)$ such that

$$\mathbf{r}_0(s_0, s_1) = \mathbf{r}_1(s_1) - s_0\mathbf{\Omega}_0, \quad s_0 \geq 0 \tag{3.27}$$

where $\mathbf{r}_0$ is any point along the path of the incident radiation before or at the point
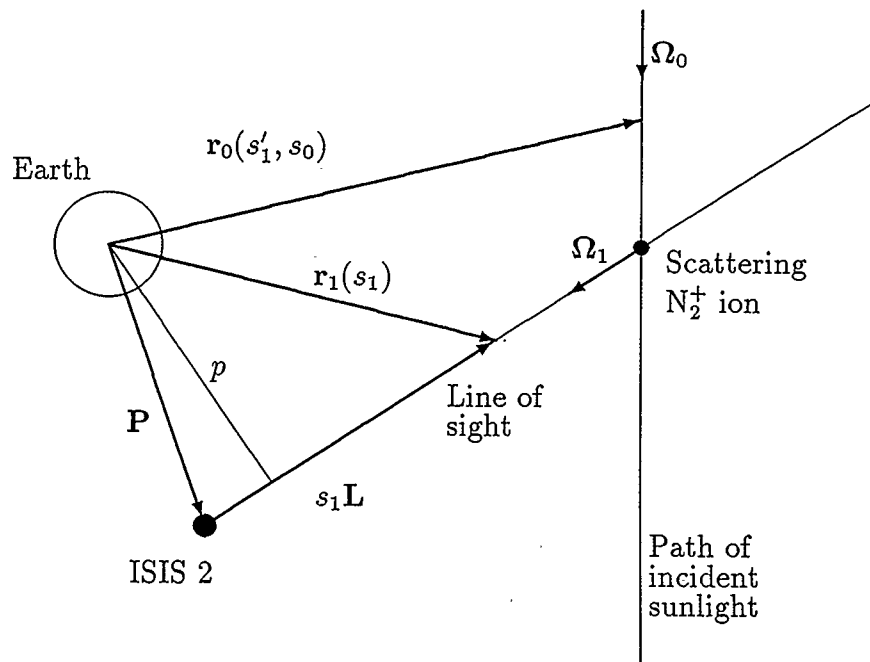
Figure 3.2: A sketch of the scattering geometry, where all vectors are in a plane containing the earth and sun and the scattering ion is located on the line of sight **L** at $s_1 = s_1'$

of scattering in the line of sight. Combining (3.25) with (3.27) gives

$$\mathbf{r}_0(s_0, s_1) = \mathbf{P} - s_0\Omega_0 - s_1\Omega_1 \qquad (3.28)$$

If we limit the vectors given in (3.25) and (3.28) to a plane which contains the earth and sun, then Figure 3.2 gives an indication of the geometry under consideration.

In this special case, where (3.22) applies, the source function along the line of sight, J_1, is proportional to the the solution of (3.26), which on the line of sight is

$$I_0(0, s_1) = I_0(\infty, s_1) \exp\left\{ -\alpha_e \int_0^\infty n(\mathbf{r}_0(s_0, s_1))\, ds_0 \right\} \qquad (3.29)$$

Applying (3.18) to this problem where local sources are neglected, $J_l = 0$, and the incident radiation is unidirectional, $I_0(r_0, \Omega) = 0$ for $\Omega \neq \Omega_0$, gives

$$J_1(s_1) = \frac{\sigma_s}{4\pi\sigma_e} p(s_1, \Theta) I_0(0, s_1) \qquad (3.30)$$

The unidirectional nature of I_0 applied to (3.19) yields, for a surface perpendicular to Ω_0.

$$F_0(s_0, s_1) = \frac{1}{\pi} I(r, \Omega_0) \qquad (3.31)$$

The definition of single scattering albedo is

$$\bar{\omega}_0 = \sigma_s / \sigma_e \qquad (3.32)$$

Combining the above definition with (3.29), (3.30), and (3.31), the following expression for $J_1(s_1)$ results

$$J_1(s_1) = \frac{\bar{\omega}_0}{4} p(\Theta) F_\infty \exp\left\{-\alpha_e \int_0^\infty n(r_0(s_0, s_1)) \, ds_0\right\} \qquad (3.33)$$

where the abbreviation $F_\infty = F_0(\infty, s_1)$ has been introduced, because, at infinity, the flux is assumed constant at its maximum value regardless of the value of s_1, and p, the phase function, is assumed to depend only on Θ.

The general solution to (3.24) is now obtained through the use of (3.33), for which formal integration yields

$$I_1(0) = \frac{1}{4}\alpha_e p(\Theta) F_\infty \int_0^\infty \bar{\omega}_0 n(r_1(s_1)) \exp\{-\tau_0(s_1) - \tau_1(s_1)\} \, ds_1 \qquad (3.34)$$

where the optical depths τ_0 and τ_1 along Ω_0 and Ω_1 respectively are

$$\tau_0(s_1) = -\alpha_e \int_0^\infty n(\mathbf{r}_0(s_0, s_1)) \, ds_0 \qquad (3.35)$$

$$\tau_1(s_1) = -\alpha_e \int_0^{s_1} n(\mathbf{r}_1(s_1')) \, ds_1' \qquad (3.36)$$

Note that the above integration utilized $e^{-\tau_1}$ as an integrating factor.

3.2.3 Airglow Photometry

A practical form of (3.34) has been developed to meet the specific requirements of airglow photometery. The goal is to remove as many physical constants from the problem as possible such that what variables remain are isolated and easily identified. For a distant source, as the Sun is for Earth, it is found that the solution can be reduced to an integration involving two variables: the number density distribution of the scattering material (N_2^+ in this case) and any matter that may participate in the collisional deactivation of the excited particles before they can radiate the absorbed light. The development begins with supposing that at some point $\mathbf{r}_1(s_1)$ along the observer's line of sight the resonant scattering of sunlight yields a directional (energy) volume emission rate, ε_ν, at some frequency ν such that over the entire absorption line the directional (photon) volume emission rate, $\mathcal{E}$, is

$$\mathcal{E}(\Omega, \mathbf{r}_1) = \int_{\text{line}} \frac{\varepsilon_\nu(\Omega, \mathbf{r}_1)}{h\nu} \, d\nu \qquad (3.37)$$

where Ω is some direction in space, and h is Planck's constant. However, it is the photons along the line of sight, $\Omega = \Omega_1$, that are of interest; thus, letting $\mathcal{J}$ denote

the flux of photons at $s_1 = 0$, *ie*, at the observer, then $\mathcal{J}$ is the sum of all the sources along Ω_1

$$\mathcal{J}(\Omega_1) = \int_0^\infty \mathcal{E}(\Omega_1, \mathbf{r}_1(s_1)) \, ds_1 \qquad (3.38)$$

Note that if $\mathcal{J}$ is measured in 10^{10} photons per square meter, per second, per steradian, then $4\pi\mathcal{J}$ is in rayleighs.

For resonant scattering, $\mathcal{E}$ can be expressed in the following particular form

$$\mathcal{E}(\Omega, \mathbf{r}_1) = n(\mathbf{r}_1) \frac{\pi F_0(0, s_1)}{h\nu} \frac{e^2}{4\epsilon_o m_e c} f(J_0 J') \bar{\omega}_0(\mathbf{r}_1, J' J_0) \frac{p(\Theta)}{4\pi} \qquad (3.39)$$

where n is the number density of the scattering particles, $\pi F_0(0, s_1)/h\nu$ is the net flux of incident photons at $\mathbf{r}_1(s_1)$ along the line of sight, and

$$\int_{\text{line}} \alpha_s(\nu) \, d\nu = \frac{e^2}{4\epsilon_o m_e c} f(J_0 J') \qquad (3.40)$$

is the integrated scattering cross section (in SI units) with e denoting the elementary charge, ϵ_o is the electrical permittivity *in vacuo*, m_e is the mass of an electron, c is the speed of light *in vacuo*, and $f(J_0 J')$ is the upward oscillator strength for the transition from a lower state J_0 to an excited state J'. The oscillator strength for the resonant scattering of 391.4 nm sunlight by N_2^+ is $f = 2.46 \times 10^{-2}$, given in [12]. The next to last term in (3.39) is the albedo for single (or primary) scattering, which was discussed above, and is, in this problem, given as

$$\bar{\omega}_0(\mathbf{r}_1, J' J_0) = \frac{A(J' J_0)}{\sum_i \{A(J' J_i) + \eta(J' J_0)[X](\mathbf{r}_1)\}} \qquad (3.41)$$

where $A(J'J_i)$ is the Einstein spontaneous emission coefficient for the transition from the excited level J' to some lower level J_i, where J_i is not necessarily the initial state J_0; $\eta(J'J_0)$ is the rate coefficient for collisional deactivation of the scattering material due to the presence of other particles, which have a number density of $[X]$. Finally, the last term, $p(\Theta)$, is the phase function that was discussed above with the definition of Θ.

Before inserting (3.39) into (3.38), the emission rate factor, g, is introduced

$$g = \pi \mathcal{F}_\infty \frac{e^2}{4\epsilon_o m_e c} f(J_0 J') \frac{A(J'J_0)}{\sum_i A(J'J_i)} \tag{3.42}$$

where $\mathcal{F}_\infty \equiv F_\infty / h\nu$, and it was given above that $F_\infty = F_0(\infty, s_1)$ for all s_1. With this definition of g, a compact expression for $\mathcal{J}$ is possible

$$\mathcal{J} = g \frac{p(\Theta)}{4\pi} \mathcal{N}_{eq} \tag{3.43}$$

where $\mathcal{N}_{eq}$ is an *equivalent* column density, which is expressed mathematically as

$$\mathcal{N}_{eq} = \int_S^\infty \frac{n(\mathbf{r}_1(s_1)) \exp\{-\tau_0(s_1) - \tau_1(s_1)\}}{1 + \Gamma(\mathbf{r}_1(s_1))} \, ds_1 \tag{3.44}$$

where S is the value of s_1 where the line of sight, $\mathbf{r}_1$, emerges from the Earth's shadow into the sunlit atmosphere; it is also possible for $S = 0$ if the observer is immersed in direct sunlight—as in the case when the observer is above the poles. The factor Γ is defined as

$$\Gamma(\mathbf{r}_1(s_1)) = \sum_i \left\{ \frac{\eta(J'J_0)}{A(J'J_i)} [X](\mathbf{r}_1(s_1)) \right\} \tag{3.45}$$

Neglecting collisional deactivation is simply the case of $\Gamma = 0$, which will be the value adopted in the data analysis, because the uncertainties in data do not warrent an investigation of $\Gamma \neq 0$. The optical depths τ_0 and τ_1 were defined above in (3.35) and (3.36), however, the form of the extinction cross section, α_s, has yet to be considered.

3.2.4 Extinction Cross Section

From spectroscopic theory, any transition from a lower state J_0 to an upper state J' due to the absorption of a photon of frequency ν has an interaction cross section

$$\alpha = \frac{e^2}{4\epsilon_o m_e c} f(J_0 J') \phi(\nu) \tag{3.46}$$

where the normalized spectral intensity distribution, ϕ, satisfies

$$\int_{-\infty}^{+\infty} \phi(\nu) \, d\nu = 1 \tag{3.47}$$

The functional form of ϕ is mainly dependent upon two physical processes: natural broadening of the line that follows from the Heisenberg uncertainty principle, and Doppler broadening due to the thermal motion of the material affecting the radiation, which in the problem of interest is thermospheric N_2^+. Natural line broadening yields a Lorentzian profile

$$\phi_L(\nu) = \frac{\Delta\nu_L/2\pi}{(\nu - \nu_0)^2 + (\Delta\nu_L/2)^2} \tag{3.48}$$

where ν_0 is the frequency at the line centre and $\Delta\nu_L$ is the full width at half maximum of $\phi_L(\nu)$ and is defined in terms of the radiative damping constant, Γ_R,

$$\Delta\nu_L = \Gamma_R/2\pi \tag{3.49}$$

with

$$\Gamma_R = \Gamma(J') + \Gamma(J_0) = 1/t(J') + 1/t(J_0) \tag{3.50}$$

where $t(J')$ and $t(J_0)$ are the mean radiative lifetimes of the material in energy levels J' and J_0 respectively. For atmospheric conditions, $\Gamma(J)$ is calculated as follows

$$\Gamma(J') = \sum_i A(J'J_i) \tag{3.51}$$

Using Einstien spontaneous emission coefficient data from [12] for the First Negative bands of N_2^+ the values of $\Gamma(J')$ and $\Gamma(J_0)$ are

$$\Gamma(J') \approx A(00) = 1.07 \times 10^7 \text{ s}^{-1} \tag{3.52}$$

$$\Gamma(J_0) = 0 \tag{3.53}$$

Using (3.52) and (3.53), then (3.49) can be evaluated

$$\Delta\nu_L = 1.703 \times 10^6 \text{ Hz} \tag{3.54}$$

Assuming thermodynamic equilibrium, the Doppler broadening gives rise to a

Gaussian line profile

$$\phi_G(\nu, T) = \lambda_0 \left(\frac{M}{2\pi kT}\right)^{1/2} \exp\left\{-(\nu - \nu_0)^2 \lambda_0^2 \frac{M}{2kT}\right\} \qquad (3.55)$$

where λ_0 is the wavelength of scattered sunlight, 3914Å, and T and M are the temperature and mass, respectively, of the N_2^+. The full width at half maximum of $\phi_G(\nu, T)$ is

$$\Delta\nu_G(T) = \frac{1}{\lambda_0} \left(\ln 2 \frac{8kT}{M}\right)^{1/2} \qquad (3.56)$$

For a typical "quiet" thermospheric temperature of $T = 900$ K, then the evaluation of (3.56) yields

$$\Delta\nu_G(900K) = 3.1 \times 10^9 \text{ Hz} \qquad (3.57)$$

Inspection of (3.54) and (3.57) reveals that $\Delta\nu_G(900 \text{ K}) \gg \Delta\nu_L$; therefore, the following simplifying approximation can be made

$$\phi(\nu) \simeq \phi_G(\nu, T \geq 900 \text{ K}) \qquad (3.58)$$

otherwise the line profile would be a convolution

$$\phi(\nu) = \int_{-\infty}^{+\infty} \phi_L(\nu')\phi_G(\nu - \nu', T)\, d\nu' \qquad (3.59)$$

The cross section (3.46) for the resonant scattering of 391.4 nm sunlight by N_2^+ can now be given as a function of frequency and temperature

$$\alpha_s(\nu, T) = \frac{e^2}{4\epsilon_o m_e c} f(J_0 J')\phi_G(\nu, T) \qquad (3.60)$$

From the definition, (3.32), of the albedo for single scattering, $\bar{\omega}_0$, along with the expression (3.10) under the condition that the scattering cross section is independent of position, gives the following relationships

$$\alpha_e(\mathbf{r}) = \alpha_s + \alpha_a(\mathbf{r}) = \frac{\alpha_s}{\bar{\omega}_0(\mathbf{r})} \tag{3.61}$$

The ratio on the far right of (3.61) is preferable when a direct measure of α_a is not possible. Instead, the formula (3.41) can be combined with (3.61) to give

$$\alpha_e(\mathbf{r}) = \left(\frac{\alpha_s}{A(J'J_0)}\right) \sum_i \{A(J'J_i) + \eta(J'J_0)[X](\mathbf{r}_1)\} \tag{3.62}$$

By inspection of (3.62), it is apparent that the extinction coefficient is not constant, but varies with the number density of particles, $[X]$, that provide for the collisional deactivation. The value of $[X]$ can usually be estimated from atmospheric models, and typically involves a single major species. At higher altitudes, $[X] \to 0$ such that $\bar{\omega}_0 \to 1$ and $\alpha_e \simeq \alpha_s$; expression (3.62) is useful when it is desired to attempt to include the upper ionosphere in an analysis of sunlight scattering. However, for exospheric observations, a useful estimate of $\alpha_e = \alpha_s$ can be made for a line using $\nu = \nu_0$ and a possible value of the thermospheric temperature in (3.55).

3.3   Upper Atmospheric Model

3.3.1   ASP Counts to Column Densities

Now that all of the quantities needed to find $\mathcal{N}_{eq}$ have been discussed, it is now possible to move on to the task of determining a conversion factor κ that transforms

raw ASP counts $\mathcal{C}$ to a column density $\mathcal{N}_{eq}$, that is

$$\mathcal{N}_{eq} = \kappa\mathcal{C} \qquad (3.63)$$

Multiplying (3.43) by 4π gives us a relationship between the measurement of the intensity, in Rayleighs (R), and the column density

$$4\pi\mathcal{J} = \frac{gp(\Theta)}{10^{10}}\mathcal{N}_{eq} \qquad (3.64)$$

where the factor of 10^{10} is needed when $\mathcal{N}_{eq}$ is in m^{-2}, and $g = 0.051$ is the emission rate factor, in photons per ion, given in [17, 68], and defined by (3.42). From the ASP calibration, we also have

$$4\pi\mathcal{J} = \eta\mathcal{C} \qquad (3.65)$$

where $\eta = 232$ R per ASP count. Substituting (3.64) and (3.65) into (3.63) yields

$$\kappa = \frac{\eta 10^{10}}{gp(\Theta)} \qquad (3.66)$$

Note that only $p(\Theta)$ and $\langle\mathcal{N}_{eq}\rangle$ are model dependent variables, with the former being constant for a given line of sight, and the latter being an estimate of the mean value of the equivalent column density given by

$$\langle\mathcal{N}_{eq}\rangle = \frac{1}{\xi}\int_{\alpha}^{\alpha+\xi}\mathcal{N}_{eq}(\alpha')d\alpha' \qquad (3.67)$$

where ξ is the angular extent of the ASP field of view, α is the *scan angle* of the ASP line of sight measured from the ISIS orbital plane in the direction of the the

satellite's spin. A practical method of evaluating (3.67) employs a local polynomial approximation to the model generated $\mathcal{N}_{eq}$, which is calculated at a series of α that are spaced regularly in time. Given that we do not expect the precision of ASP observations to be all that high and that the model count calculation is based upon many simplifying assumptions, setting $p(\Theta) \equiv 1$ for all Θ will be a negligible source of error in the estimation $\mathcal{N}_{eq}$ for an assumed distribution, $n(\mathbf{r})$, of N_2^+; this gives a conversion factor of

$$\kappa = 4.55 \times 10^{13} \text{ m}^{-2} \text{ per ASP count}$$

The problem of constructing $n(\mathbf{r})$ will be considered next.

3.3.2 Ion Distribution

Given that the solution of the radiative transfer problem will require lengthy computer numerical analysis, then it would be advantageous to keep the assumed ion distribution as simple as possible. To this end, we can avoid the development through the Boltzmann transport equation by assuming that the gas of interest is in equilibrium and isothermal. First we should look at the possibility of a real thermosphere being isothermal, or even approximately isothermal, over a useful range of altitudes. Empirical data back up this assumption, as can be found in [28], or in the appendices of [55], to the extent that within several degrees Kelvin, the thermosphere is isothermal above 300 km. Granted, the models cited are for neutral gases; however, we expect the thermosphere in equilibrium to be neutral, that is, the number density of all ions is equal to the electron number density.

The isothermal assumption is inappropriate during a thermospheric disturbance if one has observations that allow for the identification of temperature variations. It must be stressed that the ASP observations are essentially integrations of activity (resonant scattering) occuring over thousands of kilometers of space. Evidence of structural variations, other than those to be considered below, is lost in the smoothing effects of the integration. While we recognize the weakness of the isothermal assumption, we cannot ignore the futility of trying to extract more information from our observations than the data can provide.

This derivation of the ion distribution is based on the idea of *chemical potentials*. First the fundamental reaction that provides for the N_2^+ ions is considered

$$N_2^+ + e^- \rightleftharpoons N_2 \quad .$$
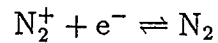
The above reaction is assumed to proceed in either direction at equilibrium, such that no changes in pressure or temperature occur. We then take the Gibbs free energy to be at a minimum in this equilibrium, and then, as in [34], the *law of mass action* follows

$$\sum_{i=1}^{3} \nu_i \mu_i = 0$$

where the numbers ν_i are the *stoichiometric coefficients* of the reaction, the μ_i are the chemical potentials of the species involved in the reactions. Let the index $i = 1$ denote quantities related to the ions, let $i = 2$ refer to the electrons, and let $i = 3$ refer to the molecules; then the law of mass action becomes

$$\mu_1 + \mu_2 = \mu_3 \qquad (3.68)$$

Each of the μ_i are functions of space and time. We suppose that there are radial variations only, and we assume that the chemical potential μ_3 of the N_2 molecules is constant. The distribution of N_2 is static if μ_3 does not vary, which is a reasonable assumption. However, it now follows from (3.68) that the sum $\mu_1 + \mu_2$ is also constant; thus, if the sum is known at some radius r_O, then at any radius r

$$\mu_1(r) + \mu_2(r) = \mu_1(r_O) + \mu_2(r_O) \tag{3.69}$$

The chemical potentials of both the ions and the electrons are similar, in that they are the sum of internal and external potentials. Given the rarefied gaseous environment in the upper atmosphere, then the internal chemical potential, μ_{int}, can be taken to be that of an ideal gas

$$\mu_{\text{int}} = kT \ln \left\{ \frac{n}{n_Q} \right\} \tag{3.70}$$

where k is Boltzmann constant, T is the temperature of the gas of number density n, and n_Q is the *quantum concentration*

$$n_Q = \left(\frac{mkT}{2\pi\hbar^2} \right)^{3/2}$$

with m being the particle's mass, and $\hbar$ Planck's constant over 2π. For an ideal gas: $n \ll n_Q$. The external part of the potential, μ_{ext}, is due to external force fields, which we will take to be gravitational and electrical

$$\mu_{\text{ext}} = \frac{GMm}{r} + q\phi \tag{3.71}$$

where G is the gravitational constant, M is the mass of the earth, q is the particle's charge, and ϕ is the electric potential at the point of interest. Using (3.70) and (3.71), then the total chemical potentials of the ions and electrons are

$$\mu_1 = kT \ln \left\{ \frac{n_1}{n_{Q1}} \right\} + \frac{GMm_1}{r} + q_1 \phi \tag{3.72}$$

$$\mu_2 = kT \ln \left\{ \frac{n_2}{n_{Q2}} \right\} + \frac{GMm_2}{r} + q_2 \phi \tag{3.73}$$

Substituting (3.72) and (3.73) into (3.69) yields an expression for the product of the ion and electron number densities, from which ϕ is absent because the charge of the N_2^+ ions is equal in magnitude and opposite in sign to the charge of the electrons

$$n_1 n_2 = n_{01} n_{02} \exp \left\{ \frac{GM(m_1 + m_2)}{kT} \left(\frac{1}{r} - \frac{1}{r_0} \right) \right\} \tag{3.74}$$

where $n_{01} = n_1(r_0)$ and $n_{02} = n_2(r_0)$. Assuming charge neutrality, $n_1 = n_2$, and utilizing the fact that $m_1 \gg m_2$, then (3.74) reduces to

$$n_1 = n_{01} \exp \left\{ \frac{GMm_1}{2kT} \left(\frac{1}{r} - \frac{1}{r_0} \right) \right\} \tag{3.75}$$

Hence, the mixture of ions and electrons behave as a neutral gas with a mass of approximately half that of the neutral parent N_2. The temperature is not the usual definition—it is only claimed that the ionized gas is expected to be distributed like a neutral gas with a temperature T; however, even early observations, such as [50], revealed that the temperature of the electrons T_e is usually greater than that of the ions T_i. Therefore, we adopt the concept of an *effective plasma temperature*, which

is clearly defined in [55]

$$T = \frac{T_i + T_e}{2} \tag{3.76}$$

The temperature that will be found in the data analysis will be interpreted as (3.76)—the average of the ion and electron temperatures. It should be stressed once again that the exact behavior of the ionized gas is not being considered, because this would entail non-equilibrium equations of state for a minor ion, as discussed in [47, 60]. Instead, we are seeking to evaluate the *average* properties of the gas.

With this aim, we can also roughly account for the decrease in the ion density as we continue below r_0 past the observed density maximum. We can roughly approximate a Chapman layer with a translated cosine function, which has its maximum set to unity at r_0 and its minimun set to zero at $r_i \approx 80$ km, where r_i is the lower bound of the ionosphere. In effect, we multiply (3.75) by the function

$$g(r) = \frac{1}{2} - \frac{1}{2}cos\left(\frac{r - r_i}{r_0 - r_i}\pi\right) \tag{3.77}$$

over the range $r_i \leq r \leq r_0$. Below r_i, we simply set $n(r) = 0$. Thus, we emulate—to a crude approximation—the observed properties of the lower ionosphere. A plot of $\log_{10}\{n(r)/n(r_0)\}$ is shown in Figure 3.3 for different temperatures.

Since (3.75) is independent of ϕ, then even if ϕ should vary with r, the charges in the gas are not affected by the electric field. This is also true even for higher orders of ionization, because the stoichiometric coefficients are such that the electric potential dependence vanishes.

However, we should not be deceived by the absence of ϕ from the earlier equation
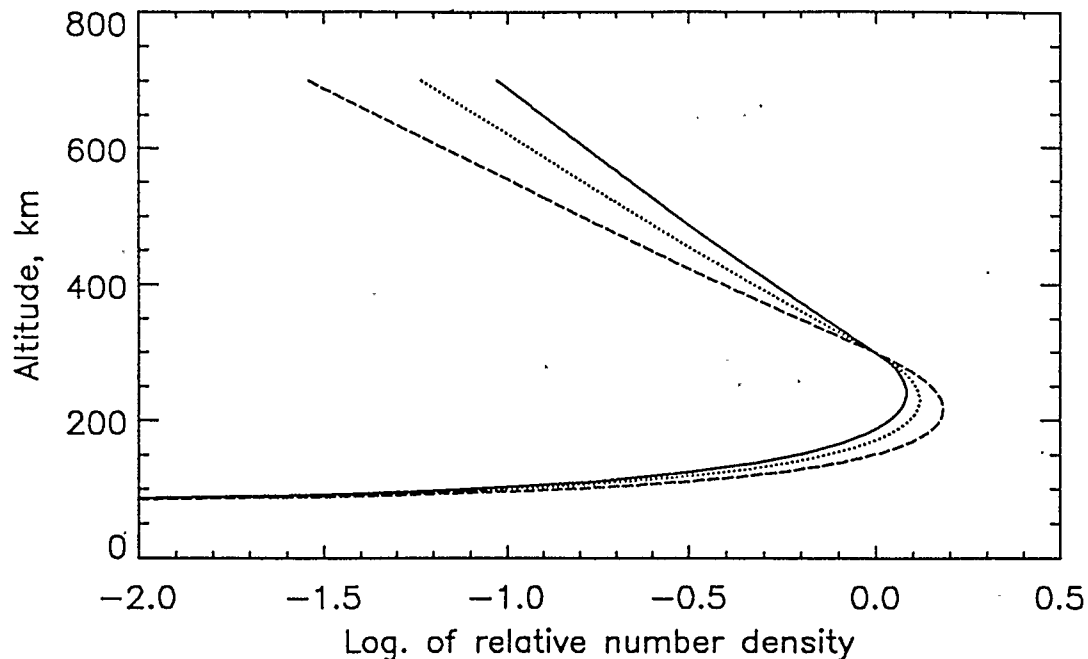
Figure 3.3: The relative number density as a function of altitude. The solid line is $T = 2400\text{K}$, the dashed line is $T = 1600\text{K}$, and the dotted line is $T = 2000\text{K}$.

(3.74). Suppose that $n_1 \neq n_2$, then the charge density ρ is

$$\rho = e(n_1 - n_2)$$

which can be applied to (3.74) to give the following expression for n_1

$$n_1 = \frac{\rho}{2e} + \sqrt{\frac{\rho^2}{4e^2} + n_{01}\left(n_{01} - \frac{\rho_0}{e}\right)\exp\left\{\frac{GMm_1}{kT}\left(\frac{1}{r} - \frac{1}{r_0}\right)\right\}} \qquad (3.78)$$

where $\rho_0 = \rho(r_0)$., and ρ must satisfy Poisson s equation. Therefore, an electric field will affect the distribution of N_2^+ at some r if and only if $\rho \neq 0$ at r. It should also be pointed out that (3.78) applies to a static situation only; there may exist unbalanced charge and electric fields, but there is no net current.

3.4 Elementary Tomography

The tomographic inversion of photometric observations made from satellites is outlined in [65, 66], which is based upon the early works on the mathematics of tomography, such as [20, 21]. The idea behind tomography is that if one knows the line integrals of a function in a plane (ideally, we know an infinite number), then one can invert the problem to provide the form of the function in the plane. Unfortunately, the ASP observations of the 391.4 nm limb number far less than infinity and are subject to random noise and systematic errors. Thus, it is all but useless to attempt to recover an image of the ASP scan plane of the quality one finds in tomographic images produced in medical applications. The poor results reported in [65, 66] were obtained from data far superior to that provided by ISIS 2; hence, we will attempt a more elementary tomographic inversion.

If we limit our analysis to regions of the upper atmosphere where we can expect it to be optically thin $\tau < 0.1$, then (3.44) reduces to

$$\mathcal{N}_{eq} = \int_S^\infty n(\mathbf{r}_1(s_1)) \, ds_1$$

Note that $\mathbf{r}_1(s_1)$, which has its functional form given by (3.25), reaches a minimum length p, also called the tangential height of the line of sight (see Figure 3.2), for some value of s_1. For any particular ISIS 2 spin, the observations can be ordered as a function of p. If we assume that the ASP is at a great distance from the scattering atmosphere, then

$$\mathcal{N}_{eq}(p) = \int_{-\infty}^\infty n(r(s_1, p)) \, ds_1$$

In addition, since the number density is assumed to vary with radius r only, then a change of variables is in order. From (3.25), the replacement of s_1 with r as the variable of integration yields

$$\mathcal{N}_{eq}(p) = 2 \int_p^\infty \frac{r n(r)}{\sqrt{r^2 - p^2}} \, dr \tag{3.79}$$

The result (3.79) is an *Abel integral equation*. The inversion, or solution, of (3.79) is discussed briefly in [5] and in detail in [26]. That is, a change of variables and then the application of both the Laplace transform and its convolution theorem to (3.79) yields

$$n(r) = -\frac{1}{\pi} \int_p^\infty \frac{\frac{d\mathcal{N}_{eq}}{dp}(p)}{\sqrt{p^2 - r^2}} \, dp \tag{3.80}$$

This method of determining the radial number density profile $n(r)$ can be compared to the method presented above; however, it can only be applied to the optically thin portion of the ASP scan. This is the problem, because even though the path along the line of sight may satisfy $\tau < 0.1$, the path of the incident sunlight does not. Hence, we can only hope for agreement to the same extent that the premises of the two models coincide.

Chapter 4

Data Analysis

4.1 Systematic Errors

After an extensive preliminary inspection of the data, it was found that the accuracy to which the data was ordered was less than that required by the radiative transfer model discussed above. The uncertainty of the actual location, in space, of the satellite is negligible compared to the uncertainties in the quantities we shall discuss next. The systematic errors in the ASP data are nontrivial and must be acknowledged before the validity of any experimental result is to be considered.

4.1.1 Line of Sight

Let $\mathbf{L}$ denote the unit vector of the line of sight of the ASP as a function of time. It is known that $\mathbf{L}$ is always perpendicular to the satellite's spin axis. Hence, once the spin axis vector is determined, the specification of $\mathbf{L}$ is a matter of computing a reference angle and a spin rate. However, if there is an error in the spin axis orientation, then there will be an error in $\mathbf{L}$.

We shall, for the moment, ignore any error in the spin axis vector, and consider the problem of correcting for systematic errors in the reference angle α_0 and the spin rate ω. That is, $\mathbf{L}$ is given by

$$\mathbf{L}(t) = \mathbf{b}_1 \cos \alpha(t) + \mathbf{b}_2 \sin \alpha(t)$$

47

where the unit vectors b_1, b_2, and b_3 form an orthonormal basis for the ISIS 2 spin orientation; b_3 is the ISIS 2 spin axis, b_1 is perpendicular to b_3 and in the satellite's orbital plane, and b_2 follows from the requirement that the three basis vectors be mutually orthogonal. The scan angle α is given by a previously written computer programme as a function of time

$$\alpha(t) = \omega(t - t_0) + \alpha_0 \tag{4.1}$$

where t_0 is the reference time. Higher order terms, such as angular acceleration, may be present; however, in the event to be examined, terms of higher order than ω were found to be zero.

Now suppose that there exist small systematic errors in ω and α_0, and let us denote these errors, respectively, as $-\delta\omega$ and $-\delta\alpha_0$; thus the corrected scan angle α_{corr} is given by

$$\alpha_{\text{corr}}(t) = (\omega + \delta\omega)(t - t_0) + (\alpha_0 + \delta\alpha_0) \tag{4.2}$$

We seek some function $f(t)$ such that

$$\alpha(f(t)) = \alpha_{\text{corr}}(t) \tag{4.3}$$

That is, (4.3) defines a transformation $f(t)$ such that the scan angle function (4.1) derived from the 557.7 nm data is now the correct angle α_{corr}. Inserting (4.1) and (4.2) into (4.3) yields

$$f(t) = t + \frac{\delta\omega(t - t_0) + \delta\alpha_0}{\omega} \tag{4.4}$$

Result (4.4) provides us with the means to avoid the repeated computation of model ASP scans. The numerical analysis is performed once for each temperature and reference number density, and then in a minimization procedure $\delta\omega$ and $\delta\alpha_0$ are variable parameters for which best fit values are sought. The time at which a model ASP observation is calculated is then transformed according to (4.4), and since all other quantities of interest, such as the geometry of L, are functions of time, they are similarly transformed. If a correction $\delta\dot{\omega}$ for angular acceleration is to be included, then (4.4) becomes

$$f(t) = t + \frac{\delta\dot{\omega}(t - t_0)^2 + \delta\omega(t - t_0) + \delta\alpha}{\omega} \tag{4.5}$$

It will be found, however, that $\delta\dot{\omega}$ will not improve the best fit to any significant amount; therefore, the inclusion of correction terms of higher order than $\delta\dot{\omega}$ is unwarranted.

The 13 element average (one data frame, see Figure 2.2) of the ASP data is plotted in Figures 4.1 and 4.2 for spins 5 and 9 respectively. The line of sight is on the Earth for the earlier times, and in the limb for the later. Therefore, we expect that the observations of interest end at the highest time for which acceptable data is available. The problem is determining where, in time, the observations of interest begin. Note that in Figure 4.1 there is a prominent peak; this feature is due to auroral emissions and this interpretation is backed up by the fact that the line of sight is near the earth's surface at the time the peak is observed—when the corrections (defined in (4.4) and determined by a best fit analysis) are applied to the line of sight, it is on the earth. There is a similar, but less obvious, feature in
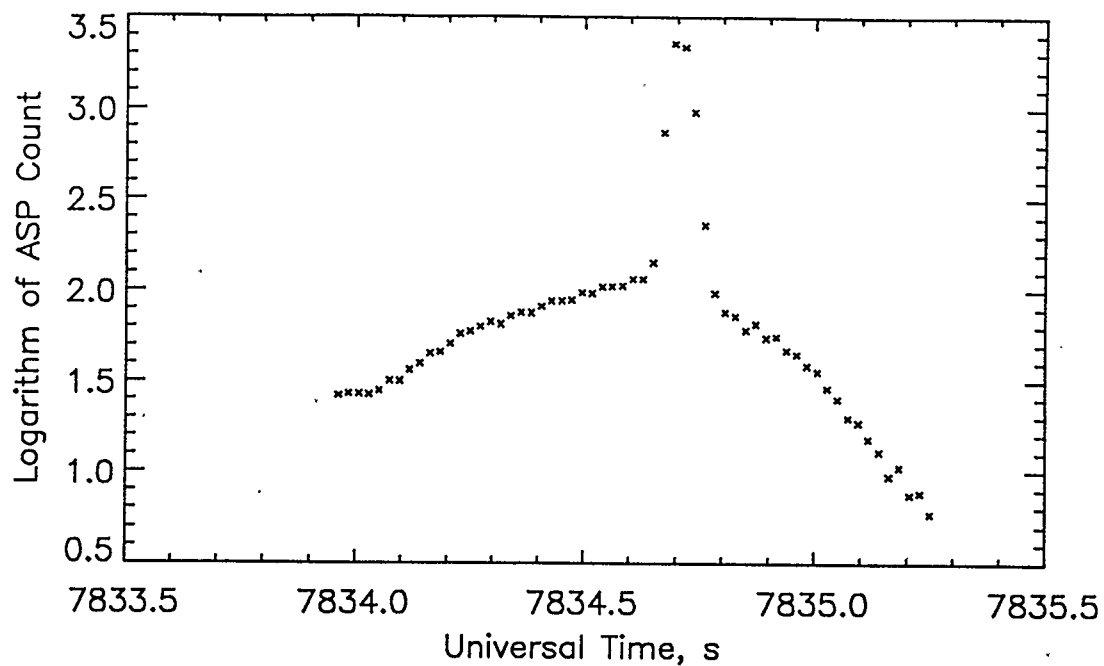
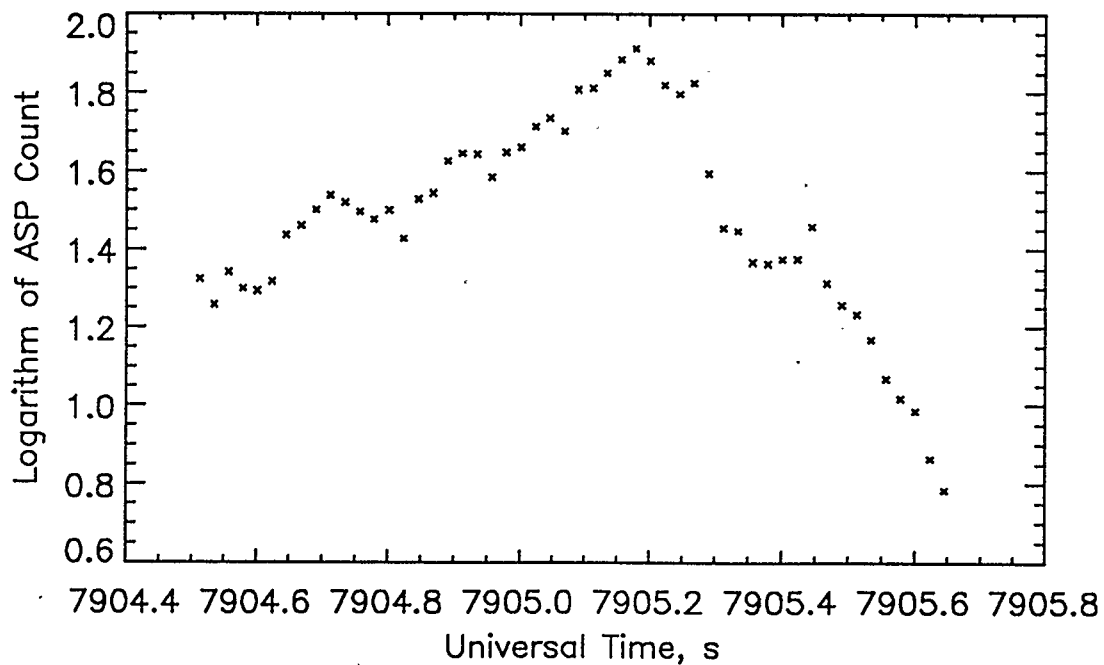Figure 4.1: ASP counts as a function of time for spin 5

Figure 4.2: ASP counts as a function of time for spin 9

Figure 4.2, supporting the interpretation that the maximum ASP count for either spin is due to the observation of an auroral feature; it appears to be a discrete arc in spin 5, and a more diffuse one in spin 9.

4.1.2 ASP Count

The calibration of the ASP before launch is discussed in [3]. Further refinements were made, such as the correction for the higher spin temperature of N_2^+ as mentioned in [73] based on the results of [14]. The uncertainties in the raw ASP count were found by [3] to match that which is expected for counting, or Poisson, statistics. The systematic errors that we are interested in cannot be accounted for before the satellite was launched, simply because the harsh orbital environment, as well as the trauma of the launch, provide for the degradation of the ASP data collection.

The updated calibration will be used as a first estimate of the sensitivity of the ASP. We will then correct for background noise $\delta\mathcal{N}_0$ and correct also for changes in the sensitivity $\delta\mathcal{N}_1$. Thus, the equivalent column density, given by (3.44) is transformed to a corrected value $\mathcal{N}_{\text{Corr}}$, as follows

$$\mathcal{N}_{\text{Corr}} = (1 + \delta\mathcal{N}_1)\mathcal{N}_{eq} + \delta\mathcal{N}_0 \qquad (4.6)$$

The background noise is estimated from ASP observations when **L** is directed away from the earth. On average, $\delta\mathcal{N}_0$ was found to be

$$\delta\mathcal{N}_0 = +1.9 \times 10^{13}\text{m}^{-2}$$

which corresponds to about 0.42 ASP counts. For the values of column densities of interest, this background is negligible.

The correction $\delta\mathcal{N}_1$ cannot be associated with any one major source of noise. In fact, if any of the factors in (3.66) are inaccurate, then letting $\delta\mathcal{N}_1$ vary in a best fit analysis will correct for the resultant systematic error due to all of those factors.

4.1.3 Spin Axis

The error in the determination of the ISIS 2 spin axis, b_3, falls into the realm of a systematic error. However, we shall not try to correct for this systematic error, simply because b_3 may be subject to precession about some axis that is changing with time. It would require a a large number of parameters to begin to account for both the error in the best estimate of b_3 and time variations in b_3. Thus, we shall try a different approach.

The ASP is divided into 13 cells, as mentioned above, such that observations are made parallel to b_3. This parallel scanning allows for a angular sweep of 2.4 degrees above and below the plane perpendicular to b_3. If we suppose that the actual spin axis is within about 2.4 degrees of the estimated direction (errors as large as 10 degrees have been estimated in some cases), then we can treat the observations of the 13 cells as a sample from a population that includes the observation of interest. Then we use the mean m as our best estimate of the ASP observation orthogonal to b_3 and the standard deviation of the mean σ_m as the estimate of the uncertainty of m due to both an erroneous determination of b_3 and the usual Poisson uncertainty.

4.2 Search for the Best Fit

The determination of the best fit model for a given data set can be done in a variety of ways, some of which are discussed in [49, 52]. Some methods involve knowledge of the gradients of the model function; however, given the form (3.44) of $\mathcal{N}_{eq}$, then this type of search for a minimum is not preferred. Instead, we shall opt for a reliable, but slower, algorithm that does not require the numerical integration of the gradients of $\mathcal{N}_{eq}$ in addition to the computation of $\mathcal{N}_{eq}$ itself.

In this way, the choice of the simplex method is made. What the simplex method lacks in sophistication, it makes up for in reliability. This is a desirable trait in a prototypical analysis. However, it will be found that the inevitable settling of the simplex in some multidimensional minimum does not lead to a sensible determination of the physical parameters. We will find that we must monitor the wanderings of the simplex so that it does not tumble into some meaningless minimum, such as fitting the model to the low count rate regions where the large uncertainties would allow for a good fit of almost any curve.

4.2.1 Least Squares Best Fit

The fundamental strategy adopted in this analysis is to use the simplex algorithm to minimize the reduced chi-squared, χ_ν^2, measure of the goodness of fit of the model y to the data Y. In particular, we are aiming to minimize

$$\chi_\nu^2 = \frac{1}{\nu} \sum_{i=1}^{N} \frac{|Y(t_i) - y(t_i, \mathbf{a})|^2}{\sigma^2(t_i)} \tag{4.7}$$

where N is the number of observations used in the analysis, t_i is the time of observation, $\mathbf{a}$ is the M dimensional vector of parameters to be varied in the simplex method, $\nu = N - M$ are the degrees of freedom of the fit, and $\sigma^2(t_i)$ is the variance of the mean of the observation $Y(t_i)$ made at time t_i. In principle, this algorithm is straight forward, and should yield some useful results; however the poor quality of the data can exclude such a desirable goal from the realm of possible outcomes. Because of the systematic errors discussed above, it will be found necessary to methodically discard data as we update our estimates of the elements of $\mathbf{a}$, which include the number density n_0, the temperature T, the ISIS 2 spin corrections $\delta\alpha_0$, $\delta\omega$ and $\delta\dot{\omega}$, and the calibration correction $\delta\mathcal{N}_1$. Hence, when it is recalled that $\delta\mathcal{N}_0$ has already been determined from the data, $M = 7$.

It is the process of eliminating data that makes it clear why it is χ_ν^2 and not the usual χ^2 that is being used in this least squares search for the best fit model—a consistent comparison can be made from one determination of χ_ν^2 to the next when N is altered. The first segment of data to be discarded is the noise floor. If all of the data is included, the simplex method immediately finds a deep minimum by squeezing the model down into the noise. By restricting the analysis to ASP counts greater than 4, this meaningless result can be avoided.

The next problem to face is the presence of spurious data, such as when a star is in the ASP field of view. These data are large counts that are far above the obvious data trend. We can eliminate the outlying points by imposing the following condition

$$\frac{|Y(t_i) - y(t_i, \mathbf{a})|^2}{\sigma^2(t_i)} \leq 9 \left(\chi_\nu^2\right)_{\min} \Rightarrow Y(t_i) \text{included} \tag{4.8}$$

The condition (4.8) is the same as eliminating spurious data which are more than 3 standard deviations away from the model (or mean), except that $(\chi^2_\nu)_{min}$ acts as a weighting factor on the order of unity that favours better fits. In short, we first find a minimum using all of the data above 4 ASP counts, and then impose (4.8) on the next iteration.

As our analysis provides a better identification of the limb data of interest, we can impose further restrictions on the data to be considered. Specifically, we extract the data that is associated with the range of altitudes where our model is expected to be useful. The observations of auroral forms are then the last of the data to be rejected. At last we hope that we end up with a set of data and a best fit search method that will provide a result in which we can be confident.

4.2.2 Uncertainties

.The uncertainties, both systematic and random, associated with the results of the determination of the best fit number density n_0 and temperature T preclude an accurate result; hence, the precision of our results may not give a true indication of their inherent error. For this reason, a detailed search for n_0 and T was abandoned. A coarse grid upon which $\log_{10}(n_0)$ varied in steps of about 0.5 and T varied in steps of 400 K was constructed. At values of n_0 and T in the search grid, the model $\mathcal{N}_{eq}(n_0, T)$ was computed. Holding n_0 and T constant, the simplex method would find the best fit under the imposed conditions discussed above, where all parameters other than n_0 and T are allowed to vary.

The grid surrounding the search grid minimum value of χ^2_ν was filled such that it was obvious the best fit model was contained in that neighbourhood. Next, the

nine values (eight boundary, one interior) nearest this region of the minimum were used to construct a least squares paraboloid of $\chi_\nu^2(n_0, T)$. That is, the nine points were used in a simple linear least squares determination of the six parameters that describe a paraboloid.

Let $\tilde{n}_0$ and $\tilde{T}$ denote the best fit number density and temperature, as yet unknown. We define the new variables u and v as follows

$$u = n_0 - \tilde{n}_0$$

$$v = T - \tilde{T}$$

Thus, where $u = v = 0$ we have the global minimum of the paraboloid. Now, if we rotate the u-v axes through an angle ψ, such that the coordinate axes correspond to the semi-major and semi-minor axes of the paraboloid, then we have the transformation

$$x = u\cos\psi + v\sin\psi$$

$$y = -u\sin\psi + v\cos\psi$$

The paraboloid is given by

$$f(x, y) = \frac{x^2}{A^2} + \frac{y^2}{B^2} + \chi_\nu^2(\tilde{n}_0, \tilde{T})$$

such that from all of the above relations we have

$$f(n_0, T) = c_1 n_0^2 + c_2 T^2 + c_3 n_0 T + c_4 n_0 + c_5 T + c_6 \qquad (4.9)$$

where the following parameters are found from a best fit analysis

$$c_1 = \frac{\cos^2 \psi}{A^2} + \frac{\sin^2 \psi}{B^2}$$

$$c_2 = \frac{\sin^2 \psi}{A^2} + \frac{\cos^2 \psi}{B^2}$$

$$c_3 = 2 \cos \psi \sin \psi \left(\frac{1}{A^2} - \frac{1}{B^2} \right)$$

$$c_4 = -2c_1 \tilde{n}_0 - c_3 \tilde{T}$$

$$c_5 = -c_3 \tilde{n}_0 - 2c_2 \tilde{T}$$

$$c_6 = c_1 \tilde{n}_0^2 + c_2 \tilde{T}^2 + c_3 \tilde{n}_0 \tilde{T} + \chi_\nu^2(\tilde{n}_0, \tilde{T})$$

From the definitions of c_4 and c_5 and some elementary linear algebra we obtain

$$\tilde{n}_0 = \frac{2c_2 c_4 - c_3 c_5}{c_3^2 - 4c_1 c_2} \tag{4.10}$$

$$\tilde{T} = \frac{2c_1 c_5 - c_3 c_4}{c_3^2 - 4c_1 c_2} \tag{4.11}$$

Similarly, from the definitions of c_1 and c_2 and c_3 and some algebra

$$A^2 = \frac{2}{c_1 + c_2 \pm \sqrt{(c_1 - c_2)^2 + c_3^2}} \tag{4.12}$$

$$B^2 = \frac{1}{c_1 + c_2 - A^{-2}} \tag{4.13}$$

$$\psi = \frac{1}{2} \arcsin \left\{ \frac{c_3}{A^{-2} - B^{-2}} \right\} \tag{4.14}$$

where we choose signs such that $A^2 > 0$ and $B^2 > 0$. The minimum value of χ_ν^2 follows immediately from the definition of c_6

$$\chi_\nu^2(\tilde{n}_0, \tilde{T}) = c_6 - c_1\tilde{n}_0^2 - c_2\tilde{T}^2 - c_3\tilde{n}_0\tilde{T} \tag{4.15}$$

We are now in a position to calculate the uncertainties σ_{n0} and σ_T of $\tilde{n}_0$ and $\tilde{T}$, respectively. It is convenient to rewrite (4.9) as

$$f(n_0, T) = c_1(n_0 - \tilde{n}_0)^2 + c_2(T - \tilde{T})^2 + c_3(n_0 - \tilde{n}_0)(T - \tilde{T}) + \chi_\nu^2(\tilde{n}_0, \tilde{T}) \tag{4.16}$$

The level at which we find the variables have departed from $\tilde{n}_0$ and $\tilde{T}$ by k standard deviations, is where chi-squared has increased by k^2 above its minimum value; since we are using the reduced chi-squared, then the k standard deviation level corresponds to

$$f(n_0, T) = \frac{k^2}{\nu} + \chi_\nu^2(\tilde{n}_0, \tilde{T}) \tag{4.17}$$

where $k = 1$ for one standard deviation. As discussed in [49, 52], the uncertainties are the projections of the extrema of the ellipse at the level (4.17) onto the n_0 and T axes. That is, $\sigma_T = (T - \tilde{T})$ for some T such that $\frac{\partial f}{\partial n_0}(n_0, T) = 0$ and (4.17) hold; using these conditions and (4.16), we find for $k = 1$

$$\sigma_T = \pm\frac{1}{\sqrt{\nu\left(c_2 - \frac{c_3^2}{4c_1}\right)}} \tag{4.18}$$

Similarly, the standard deviation of n_0 is

$$\sigma_{n0} = \pm \frac{1}{\sqrt{\nu \left(c_1 - \frac{c_3^2}{4c_2}\right)}} \tag{4.19}$$

We have accomplished the task of defining an algorithm to compute the best estimate and uncertainty of both n_0 and T, which are the end result of the least squares fitting procedure discussed above.

4.3 Numerical Inversion of the Abel Integral Equation

Having used the assumption that ISIS 2 is a distant observer in our derivation of (3.80), then we have a situation that is similar to a spacecraft passing by a planet. Thus, we will use a modified version of the "exponential form" data reduction suggested in [57].

4.3.1 Exponential Column Density Profile

Previous modelling revealed that, to a good approximation, the equivalent column density $\mathcal{N}_{eq}$ falls off exponentially with the line of sight tangential height p for a limited range of p. This implies that a good fitting function over this range of p is

$$\mathcal{N}_{eq} = \mathcal{N}_0 \exp\{\beta(p - p_0)\} \tag{4.20}$$

where $\mathcal{N}_0 = \mathcal{N}_{eq}(p_0)$ and both $\mathcal{N}_0$ and β are found using a singular value decomposition (SVD) algorithm to produce a stable least squares best fit. The practical aspects of the SVD approach are given in [52], and the theory is presented in [42]. The dis-

tinct advantage of the SVD algorithm is that it yields a useful solution even when the problem is *ill conditioned*. Detailed solutions of upper atmospheric radiative transfer problems are notoriously ill conditioned; various difficulties and disappointments with inversion methods are revealed in [1, 35, 65, 66]. The common conclusion is that the presence of noise, even in small amounts, provides for larger errors propagated through the inversion process. For these reasons, we will use the SVD least squares analysis in an attempt to skirt the expected obstacles.

Inserting (4.20) into (3.80) yields

$$n(r) = -\frac{\mathcal{N}_0 \beta e^{-\beta p_0}}{\pi} \int_r^\infty \frac{e^{\beta p}}{\sqrt{p^2 - r^2}} dp \qquad (4.21)$$

A change of variables, $p = r \sec \theta$, in (4.21) provides for an integral that is well-suited to numerical integration

$$n(r) = -\frac{\mathcal{N}_0 \beta e^{-\beta p_0}}{\pi} \int_0^{\pi/2} \sec \theta e^{\beta r \sec \theta} d\theta \qquad (4.22)$$

After determining $n(r)$ at the radii r allowed for by the observations, we can determine the temperature T by performing another SVD analysis on the data with (3.75) as the fitting function.

4.3.2 Propagation of Uncertainties

The variances $\sigma_{\mathcal{N}_0}^2$ and σ_β^2 associated with $\mathcal{N}_0$ and β can be propagated through the Abel inversion in order to provide an estimate of the uncertainty in $n(r)$. We shall use the following formula for the variance $\sigma_n^2(r)$ of $n(r)$, where the variances $\sigma_{\mathcal{N}_0}^2$ and

σ_β^2 are independent and uncorrelated

$$\sigma_n^2 = \left(\frac{\partial n}{\partial \mathcal{N}_0}\right)^2 \sigma_{\mathcal{N}0}^2 + \left(\frac{\partial n}{\partial \beta}\right)^2 \sigma_\beta^2 + \left(\frac{\partial^2 n}{\partial \beta \partial \mathcal{N}_0}\right)^2 \sigma_{\mathcal{N}0}^2 \sigma_\beta^2 \qquad . \qquad (4.23)$$

which is derived in [6, 49]. From (4.22) we have

$$\frac{\partial n}{\partial \mathcal{N}_0}(r) = \frac{n(r)}{\mathcal{N}_0}$$

$$\frac{\partial n}{\partial \beta}(r) = n(r)\left(\frac{1 - \beta p_0}{\beta}\right) - \frac{\mathcal{N}_0 \beta e^{-\beta p_0} r}{\pi} \int_0^{\pi/2} \sec^2 \theta \, e^{\beta r \sec \theta} d\theta$$

$$\frac{\partial^2 n}{\partial \beta \partial \mathcal{N}_0}(r) = \frac{1}{\mathcal{N}_0} \frac{\partial n}{\partial \beta}(r)$$

We can now turn our attention to the results of the data analysis we have designed.

Chapter 5

Results

First we shall discuss the results obtained from the method in which we account for the extinction of 391.4 nm sunlight due to N_2^+ scattering the light in directions other than the ASP line of sight. For convenience we shall refer to this method as PSE—primary scattering with extinction. Similarly, we shall name the second method, which will consider primary scattering with no extinction, PSN. Before we proceed, it would be a good idea to recognize that the uncertainties that will be associated with the results are a reflection of the precision of the methods used. The accuracy of the results is another problem altogether. Having examined our results, we shall then attempt to assess the extent to which we can be confident that they are a reflection of the actual physical conditions that provided for the ASP observations during the large magnetospheric storm on 18 December, 1971.

5.1 Primary Scattering with Extinction

The greatest obstacle to this analysis was finding a series of ISIS 2 spins over which the spin vector and rate seemed stable. The evening side observations were very near the ASP threshold; hence, very little data above 5 counts was available. At length, it was found that the evening side data added little to the analysis, and eventually it was ignored. The morning side observations provided good quality data for over 15 spins. A stable best fit temperature T and number density n_0 were found for

62

spins 4 to 10. What is meant by a stable best fit is that even when the best fit parameters were perturbed, the algorithm returned the parameters to their original values. This desirable property was an uncommon feature, and is probably the most valuable indicator of a best fit.

The best fit temperature and number density are

$$T = 2420 \pm 70\text{K} \tag{5.1}$$

$$n_0 = (2.4 \pm 0.7) \times 10^9 \text{m}^{-3} \tag{5.2}$$

Note that all densities reported have been subsequently corrected for the fraction of N_2^+ that is in the lowest vibrational state of the ground electronic state; the relevant fraction is 0.55 for an ionic temperature of about 1500 K; the data is provided in [12].

The fits are worst for the two spins at the end of the interval of interest—spins 4 and 10. Spin 10 is the poorest of them all, yet spin 9 is apparently the best. The interior spins 5 to 9 are shown in Figures 5.1 to 5.5 . One notable feature of these plots of the best fit PSE limb profiles is how the kink in the model profile, which is located at a tangential height $p \approx 80$ km in Figure 5.1, slowly moves to higher values of p in subsequent spins: $p \approx 150$ for spin 7 shown in Figure 5.3 and $p \approx 210$ km for spin 9 shown in Figure 5.5. This trend is somewhat noticeable in the observed data. The physical reason for this kink is that for lower values of p the ASP line of sight passes through the earth's shadow cylinder as ISIS 2 proceeds in its polar pass from the day side to the night side. The satellite's orbit carries it down into the penumbra, such that the apparent angular extent of the shadow cylinder increases.
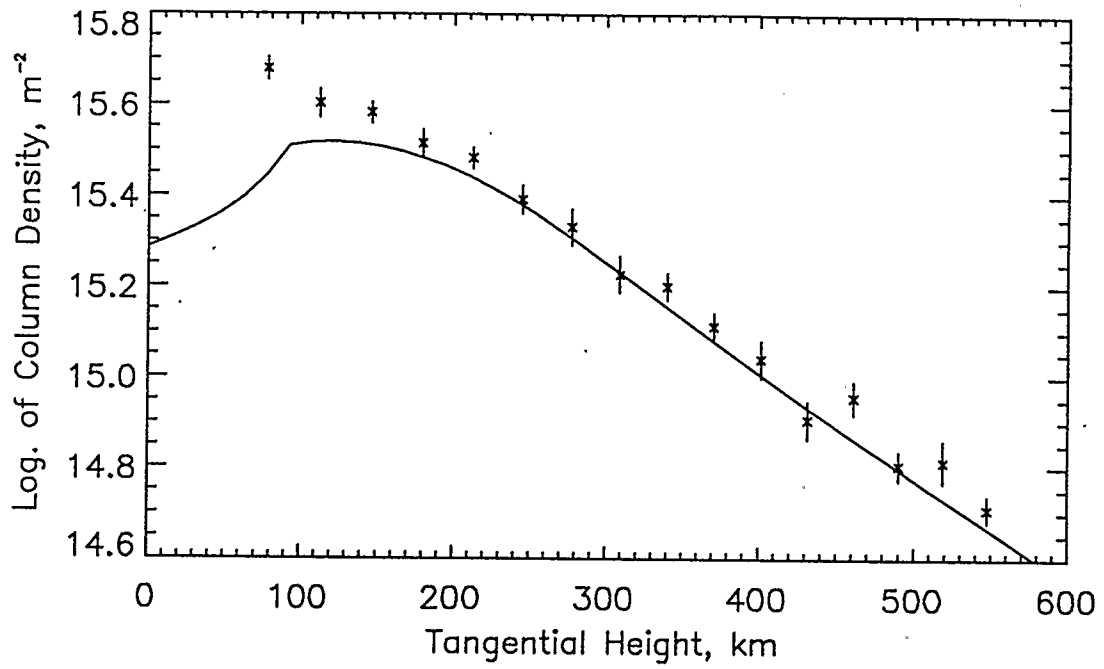
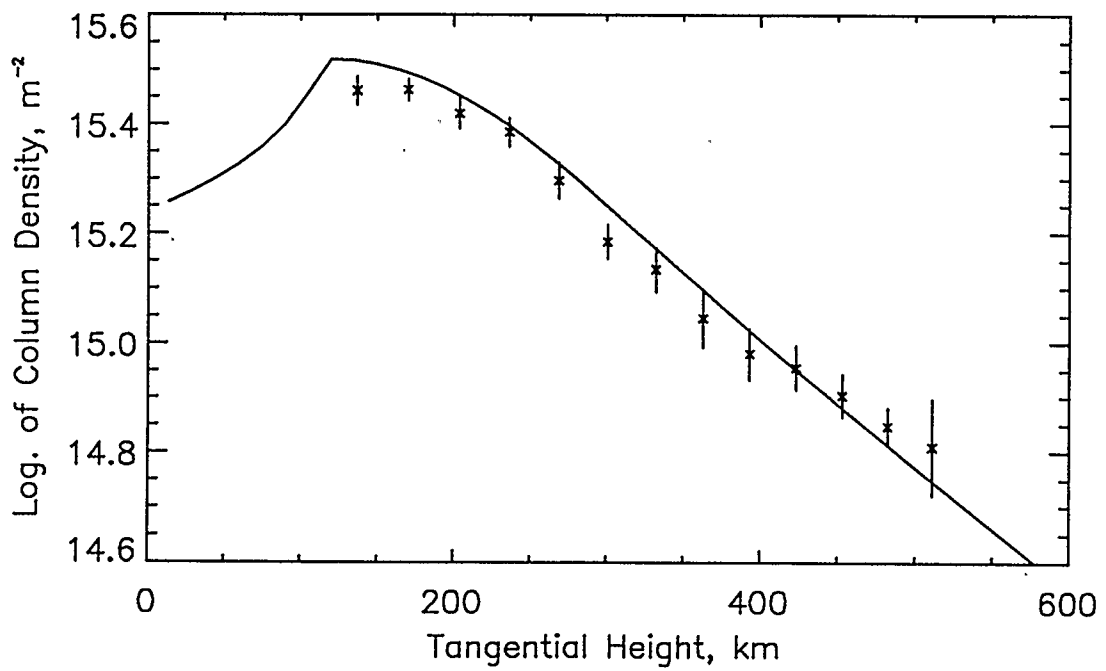Figure 5.1: PSE model best fit for the morning side—spin 5.

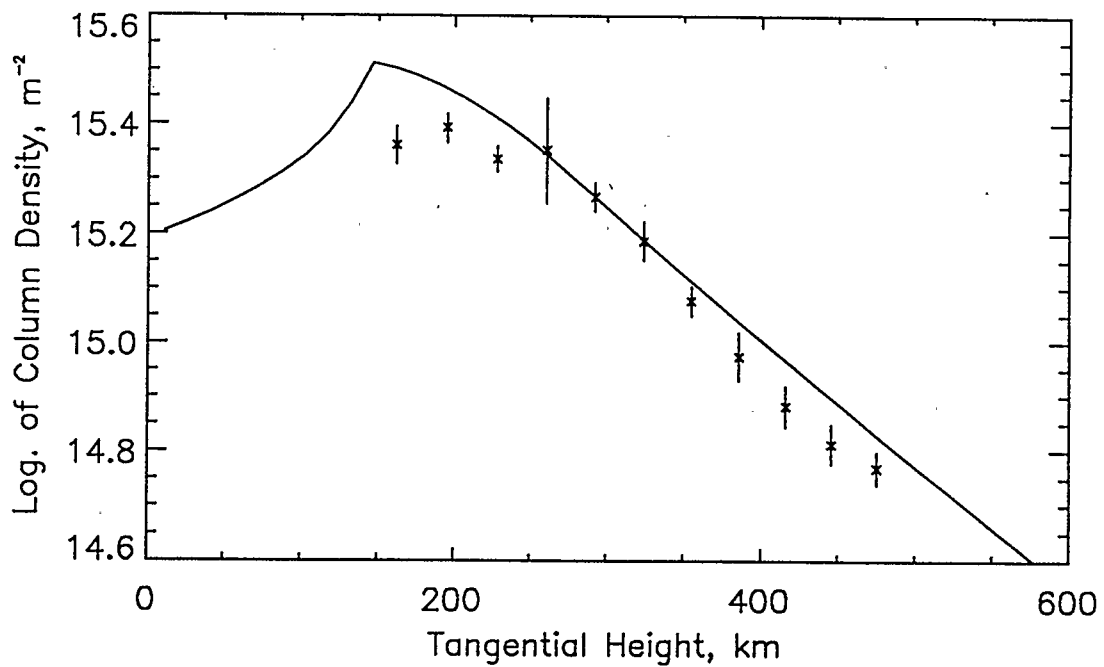Figure 5.2: PSE model best fit for the morning side—spin 6.

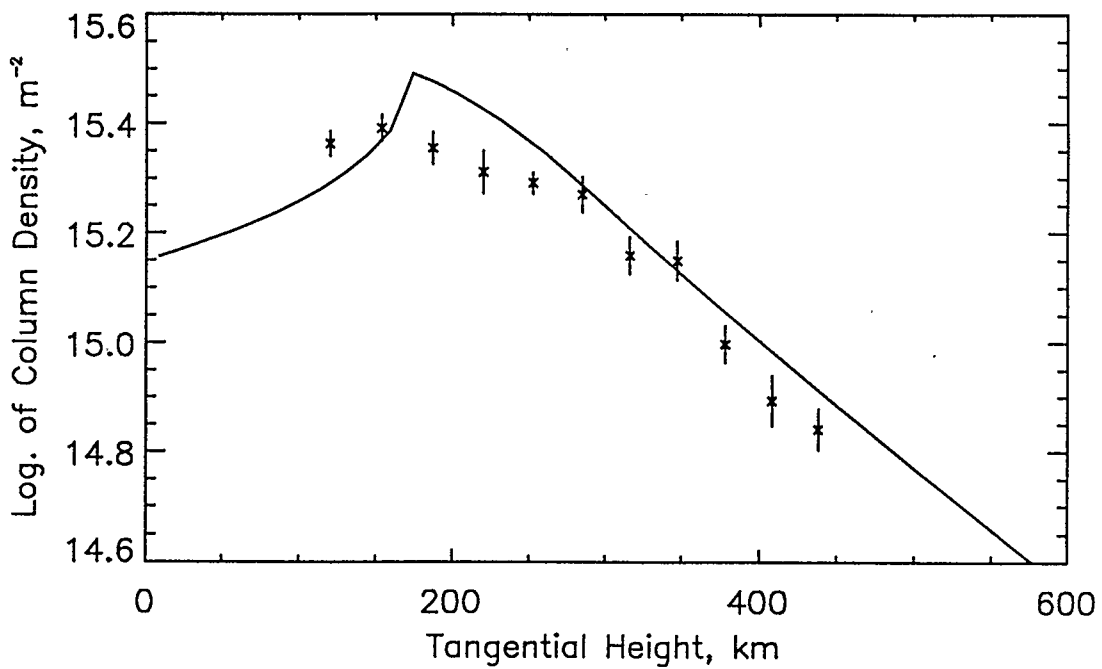Figure 5.3: PSE model best fit for the morning side—spin 7.

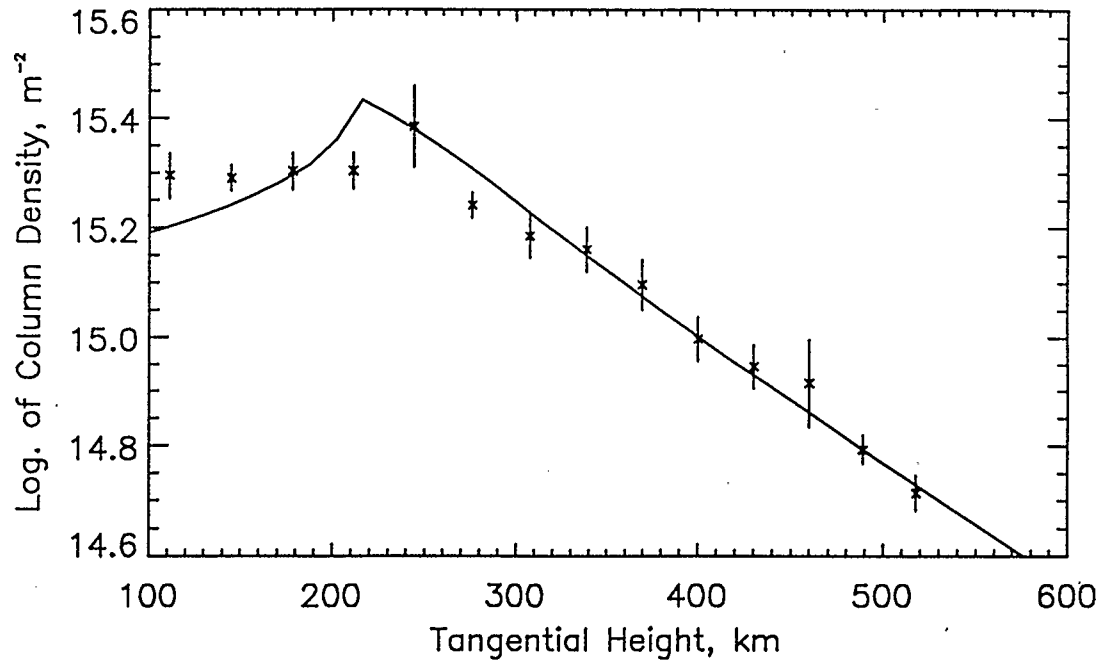Figure 5.4: PSE model best fit for the morning side—spin 8.

Figure 5.5: PSE model best fit for the morning side—spin 9.

In this way, with each passing spin, the ASP line of sight intersects with the shadow cylinder for larger and larger values of p.

The best fit values for the corrections to the reference angle $\delta\alpha_0$, the spin rate $\delta\omega$, and the ASP calibration $\delta\mathcal{N}_1$ were found to be

$$\delta\alpha_0 = -0.141\text{rad} = -8.08°$$

$$\delta\omega = -6.92 \times 10^{-4}\text{rad s}^{-1} = -3.96 \times 10^{-2}\text{deg s}^{-1}$$

$$\delta\mathcal{N}_1 = -0.624$$

The size of $\delta\alpha_0$ is far larger than the $1°$ uncertainty expected in [46] and $\delta\omega$ provides a relative uncertainty of 0.2%, whereas [46] anticipated a relative error of 0.01%.

Hence, a serious limit on the accuracy of our results is due to the processing of the data before the PSE analysis is performed. In addition, the statistics, namely the value of χ_ν^2, indicates a poor fit—either the uncertainties in the ASP counts are under estimated, or the model is incorrect. Given that the results for $\delta\alpha_0$, $\delta\omega$ and $\delta\mathcal{N}_1$ are significantly larger than expected, it is hard to decide what is the cause of the poor statistics.

5.2 Primary Scattering with no Extinction

We use the corrections $\delta\alpha_0$, and $\delta\omega$ that were found in the PSE analysis in the analysis that ignores extinction (PSN). However, if a meaningful comparison is to be made between the analyses, the inverse correction must be applied to the data. This is because the calculation of $\mathcal{N}_{eq}$ by either (3.44) or (3.79) involves no parameters related to the ASP. Hence, the observed ASP count $\mathcal{C}$ is subject to the inverse of the transformation given by (4.6) before performing the PNE analysis

$$\mathcal{N}_{eq} = \frac{\kappa\mathcal{C} - \delta\mathcal{N}_0}{1 + \delta\mathcal{N}_1}$$

The reason we shall use the corrections $\delta\alpha_0$ and $\delta\omega$ for the line of sight is apparent from inspection of Figure 5.6, where we can see that the tangential height p of the uncorrected line of sight differs significantly from that which has been corrected. For instance, at $t = 7835.0$ s Universal Time, the corrected value of the tangential height is $p \approx 200$ km, while the uncorrected value is $p \approx 400$ km. This is a significant difference; hence we will use $\delta\alpha_0$ and $\delta\omega$ in our PSN determination of T and n_0

The best fit lines to the logarithm of ASP count versus the line of sight tangential
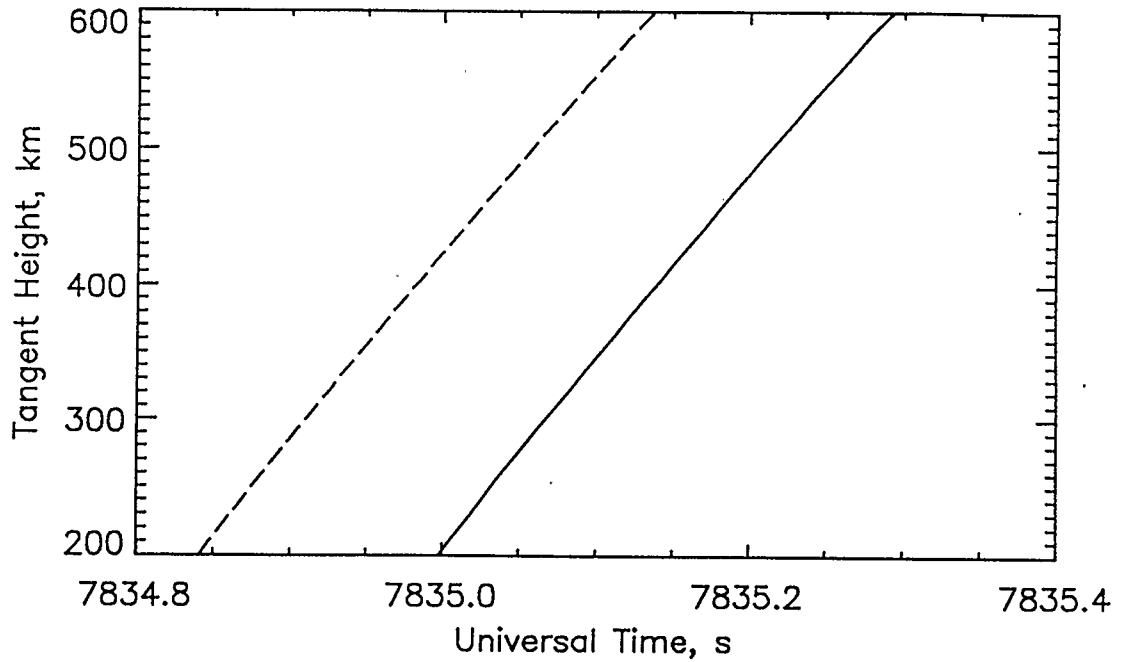
Figure 5.6: Tangential Height as a function of time. The solid line is the function due to the corrections found in the PSE analysis, the dashed line is the uncorrected form.

height are shown in Figures 5.7 to 5.11. The resulting temperatures and number densities are in Table 5.1. A plot of the inverted number density profile is uninteresting, because the exponential fit (4.20) to the column density smooths the data such that the best fit line necessarily passes through all of the points.

From the results given in Table 5.1, the weighted means and their associated uncertainties are

$$T = 2320 \pm 80\mathrm{K} \tag{5.3}$$

$$n_0 = (1.61 \pm 0.03) \times 10^9 \mathrm{m}^{-3} \tag{5.4}$$
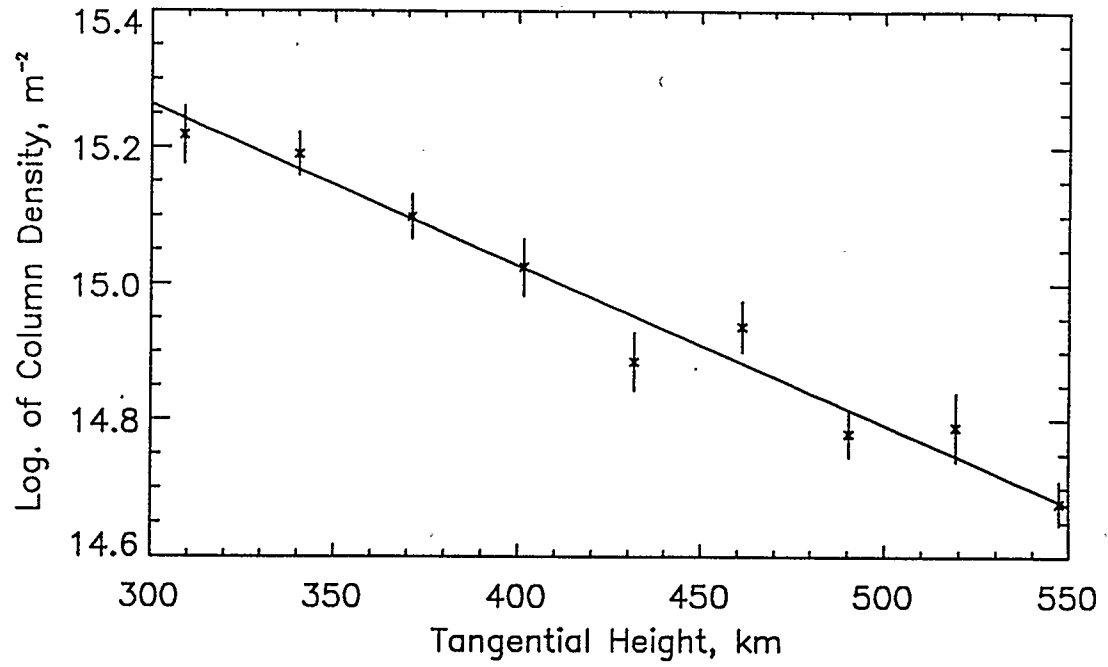
Figure 5.7: PSN best fit for spin 5 only—morning side.
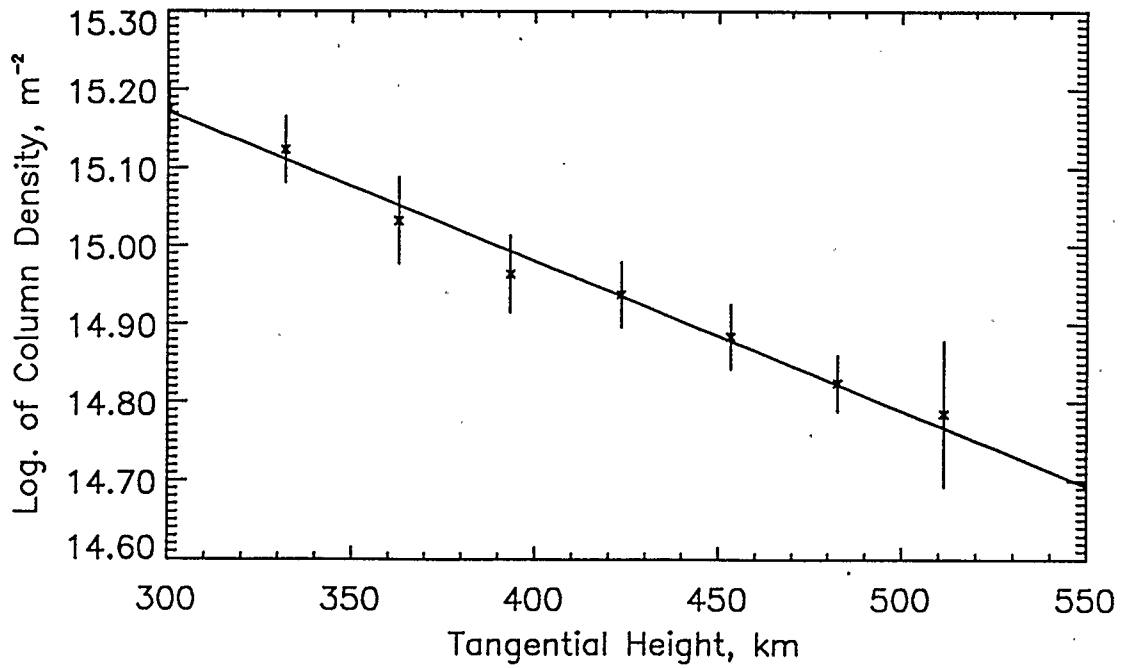
Figure 5.8: PSN best fit for spin 6 only—morning side.
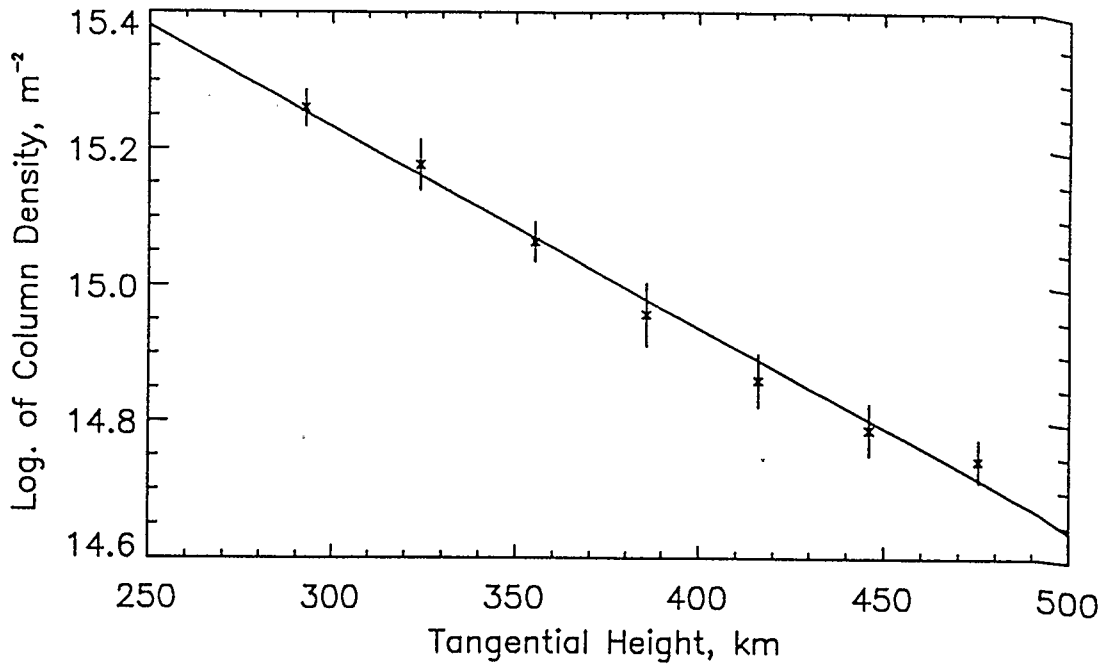
Figure 5.9: PSN best fit for spin 7 only—morning side.
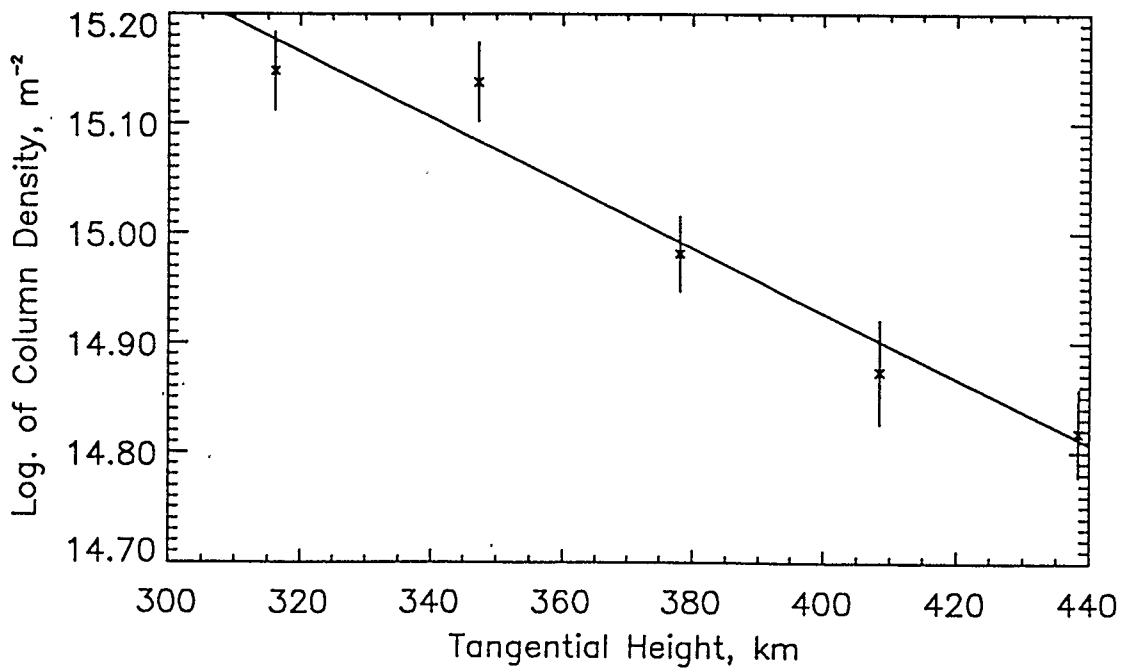
Figure 5.10: PSN best fit for spin 8 only—morning side.
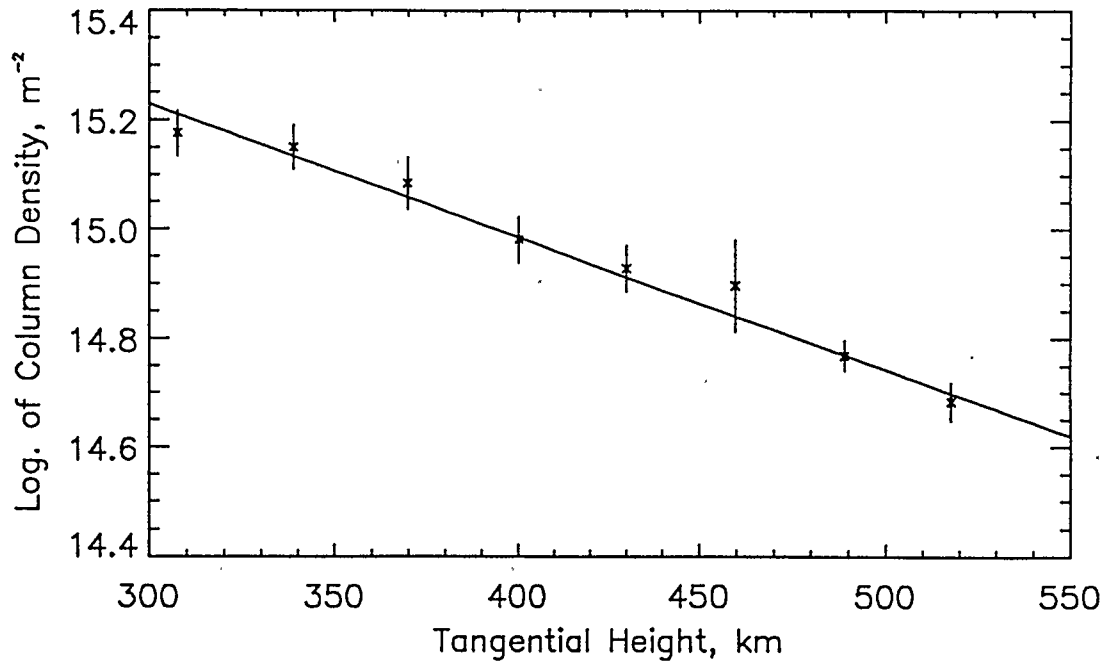
Figure 5.11: PSN best fit for spin 9 only—morning side.

SPIN #	T K	n_0 10^9 m^{-3}
5	2600 ± 200	1.72 ± 0.08
6	3300 ± 300	1.25 ± 0.08
7	2100 ± 100	1.79 ± 0.08
8	2100 ± 300	1.8 ± 0.2
9	2600 ± 200	1.61 ± 0.08

Table 5.1: Temperatures and densities from the PSN analysis.

5.3 Discussion

The precision of the results for the temperature T and the number density n_0 at 300 km we shall expect to be reflected well by the uncertainties provided by the methods used to find T and n_0. Results (5.1) and (5.2) show that for the primary scattering with extinction (PSE) analysis, the relative precision of T is $\pm 3\%$, and for n_0 it is $\pm 31\%$. Hence, we shall view our determination of the temperature to be a better estimate of the related thermal properties of the upper atmospheric N_2^+ than the estimate of the number density.

In Table 5.1 the results for the method that uses primary scattering with no extinction (PSN) are displayed. It reveals a fairly consistent result for the number density, except for spin 6, whereas, the temperatures vary widely. We expect the PSN estimate (5.4) of n_0 to be systematically lower, since the optical depth of the scattered sunlight has not been taken into account—there appear to be fewer scattering ions only because of extinction. However, the temperature is expected to be nearly the same; this is because the extinction effects are fairly uniform for limb observations over the tangential heights (300 km minimum) considered. In fact, within experimental uncertainties, the PSE result (5.1) for the temperature T agrees with the PSN weighted mean (5.3). The relative uncertainties in the PSN weighted means have a closer relationship than that noted above for the PSE best estimates: $\pm 3\%$ for T, and $\pm 2\%$ for n_0.

We shall now look at the results with the intention of finding observations that support the findings of this investigation. The observations will be from a variety of sources; most of them will be upper atmospheric temperatures and densities mea-

sured during a geomagnetic storm—not necessarily during the storm of 18 December, 1971. We are seeking reasons to reduce our initial skepticism: facts that provide for confidence in the accuracy of the results.

5.3.1 Temperature

First, we should clarify what is meant by temperature. Our results will be interpreted as the effective plasma temperature, as given by (3.76) to be $T = (T_i + T_e)/2$. This means that we must consider observations of thermospheric electron temperatures T_e, as well as ion temperatures T_i during geomagnetic storms. In addition, the neutral particle temperature T_n will also be examined, because of the well established result, provided in [55], that the temperatures of interest are related as follows

$$T_n \leq T_i \leq T_e \tag{5.5}$$

From the relationship given by (5.5), and the fact that observations of T_n are more common than those of T_i—and far more so than the temperature of N_2^+ in particular—then we will consider some measurements of T_n so as to establish a typical lower bound on T_i.

Even the earliest results of observations from rocket borne experiments agree with the results of this analysis. In [50], it was found that during the magnetic storm of 3 August, 1962, the daytime temperatures of interest above 300 km were $T_i \approx 1600$ K and $T_e \approx 3000$ K; an effective plasma temperature of 2300 K results. The observations cease at about 350 km, so that no conclusion can be drawn as to what degree the thermosphere was isothermal. During a different storm on the same

day, oddly enough, but two years earlier in 1960, [10] found an isothermal (within 10%) electron temperature of $T_e \approx 3000$ K between the altitudes of 300 and 400 km. This was compared with a quiet day temperature of $T_e \approx 1800$ K; hence, systematic errors in detection or data reduction seem remote. No value of T_i was reported.

Although ground based incoherent radar measurement of upper atmospheric temperatures are less direct (the data reduction depends on assuming the unknown ion composition and distribution), there is also no stark inconsistencies with our results. Some observations made during sunspot minimum and geomagnetically quiet conditions are presented in [23]. At 300 km it was found that $T_i \approx 800$ K and $T_e \approx 2200$ K. Thus, even during quiet conditions, the ion and electron temperatures are definitely different. It was also found that the temperatures increased significantly with height, such that by 600 km they were calculated to be $T_i \approx 1700$ K and $T_e \approx 3000$ K, which are typical temperatures measured by the rocket experiments during disturbed conditions. This observation certainly weakens the soundness of our assumption of an approximately isothermal thermosphere; however, radar based calculations of temperature become less certain with increasing altitude, because errors in the assumed ion distribution also accumulate.

A comparison of radar observations of the same disturbed ionosphere by two different stations was presented in [54]. The temperatures at 300 km were $T_i \approx 1700$ K and $T_e \approx 3100$ K such that $T \approx 2400$ K, which agrees well with our result. There was also a discussion of a systematic difference of about 200 K between the two stations, but this was seen to be less worrisome than the large uncertainties introduced by the required conjecture regarding the arrangement of ions with altitude.

A Fabry-Perot spectrometer was used by [32] to observe a neutral thermospheric

temperature of $T_n \approx 1600$ K during the geomagnetic storm of 2 March, 1983. This was the peak temperature, and according to (5.5), it gives us a lower bound on the typical T_i associated with a thermospheric disturbance, and it is not inconsistent with the ion temperatures discussed so far.

Satellite observations of the upper atmosphere provide another important test of our result. Our assumption of a roughly uniform thermospheric temperature independent of longitude or latitude was found to be in disagreement with the findings of [37], where it was concluded that the upper atmospheric temperature increases from the geomagnetic equator, and reaches a peak in the auroral zone. However, it was also found that this temperature gradient dissipates with the propagation of a density wave from the higher auroral latitudes toward the lower—more about this in our discussion of densities. ISIS 2 electron temperatures at 1400 km (orbital altitude) during the 18 December, 1971 large storm, which is our event of interest, are presented in [15]. During spins 5 to 9 on orbit 3306, the electron temperature is scattered widely about $T_e \approx 3000$ K; since other observations lead us to expect the electron temperature to increase with altitude, this observation gives an upper bound estimate on the electron temperature of the event we have analyzed. Unfortunately, ion temperatures at the ISIS 2 orbit could not be measured, as the instrument was useless when the ASP was collecting data by scanning perpendicular to the orbital plane. In [11], ISIS 2 temperatures are reported for a different storm; the electron temperature stayed in the range of 3000 to 4000 K, even to lower latitudes, whereas the ion temperature was highly variable, and it reached a peak of 3000 K at about 50 degrees geomagnetic latitude (1400 km altitude).

The measurements of the Dynamics Explorer 1 satellite also show a lack of vari-

ation in T_e with latitude, where the observations are at altitudes lower than ISIS 2 : about 700 to 1000 km. However, large variations in T_e were found to be associated with the crossing of localized magnetospheric features, such as the plasmapause. At these thermospheric altitudes, it was found that $T_e \approx 1500$ K at quiet times to $T_e \approx 4000$ K at disturbed times. Another result from the Dynamics Explorer concerns a solar proton event, 13 July, 1982, where [58] provide a neutral thermospheric temperature over the poles of $T_n \approx 2000$ K, which gives us an extreme measurement of T_n that is not commonly found in geomagnetic storms.

So far we have discussed observations made on the day side, in direct sunlight, but our results follow from observations of the morning side limb. Night side observations during large storms show systematically lower temperatures in the thermosphere; however, the temperatures are seen to be step functions, as reported by [56], where the twilight temperatures change nearly instantly from one extreme to the other. During quiet upper atmospheric conditions, the step in temperature can be 1000 K or more for electrons, less for ions. Disturbed periods, in contrast, are characterized by higher temperatures and smaller day and night differences. Of course, the polar thermosphere, which is of chief interest, is always in sunlight, and so twilight temperature behaviour is of interest only for the lowest tangential heights of our observations—a region we are not claiming to model.

Through a different method, [73] attempted to determine the temperature of upper atmospheric ionized N_2 gas. Although [73] calculated a best fit temperature of $T \approx 1750$ K, this result was not immediately acceptable, because it was expected that the ionized gas would have the same temperature $T_\infty \approx 900$ K as the neutral thermospheric components. If we take this value of T_∞ as an estimate of the lower

bound of T_i and use a typical quiet time electron temperature, say $T_e \approx 2200$ K as given in [23], then inserting these two temperatures into (3.76) yields 1550 K as a lower bound estimate of the effective plasma temperature. Looking at the results of [73] in this way, the temperature now appears physically reasonable and acceptable.

5.3.2 Number Density

Ground based observations of thermospheric N_2^+ number densities are available; however, they tend to be searches for the emitting layer (altitude of maximum density), rather than being concerned with the determination of composition as a function of altitude. In addition, tropospheric Rayleigh scattering of 391.4 nm light, discussed in [13], all but eliminates the possibility of acquiring the observations that are necessary for detailed descriptions of density variations with altitude.

Photometers carried to lower thermospheric altitudes by rockets provide better observations than the earth bound experiments. Unfortunately, in most cases the rocket does not go as high as 300 km; instead, they end their ascent at the N_2^+ density maximum, which is at about 230 km. We shall use (3.75) to extrapolate the densities at any altitude to that which is to be expected at 300 km. For instance, [75] provides an afternoon number density of $[N_2^+] \approx 3 \times 10^9$ m^{-3} at 220 km. With a quiet temperature of the ionized gas of 1500 K, this gives an estimate of the density at 300 km of $n_0 \approx 1 \times 10^9$ m^{-3}, which is of the same order of magnitude as our PSE and PSN results. Another daytime measurement under quiet geomagnetic conditions is reported by [24], in which the rocket ascended to the 300 km level, where it was found that $n_0 \approx 6 \times 10^8$ m^{-3}. This is lower than our results, as would be expected for quiet conditions in direct sunlight. A last example is from [64], where it was

found that $[N_2^+] \approx 1 \times 10^9$ m^{-3} at 260 km; which gives $n_0 \approx 7 \times 10^8$ m^{-3}. Thus, both our PSE and our PSN results are 5 times larger than quiet thermospheric densities, which we expect to be lower bound estimates.

An upper bound estimate on our n_0 result can be obtained from the fact that the earliest detection of any N_2^+ at the ISIS 2 orbital altitude was stated in [33] to be associated with the 4 August, 1972 geomagnetic storm—none were detected during the event we have considered, because the ion mass spaectrometer was inoperative when the satellite was in orbit aligned mode. Suppose that at the orbital altitude of 1400 km the N_2^+ number density is of the same order of magnitude, 10^8 m^{-3}, as observed during the August 1972 storm. For a temperature of 2400 K, the density at 300 km is $n_0 \sim 10^{10}$ m^{-3}. This upper bound estimate indicates that our result is of an acceptable magnitude.

The number densities of about $n_0 \approx 2 \times 10^9$ m^{-3} obtained by [73] is associated with the so-called *winter enhancement* of N_2^+ in the polar thermosphere. This agrees well with our result, even though, as mentioned above, the method of analysis was different than either of the two used in this investigation. An undisturbed mid-latitude density measurement, by satellite, of $[N_2^+] \approx 1 \times 10^9$ m^{-3} at 225 km is recorded in [70], which can be extrapolated to 300 km to give $n_0 \approx 5 \times 10^8$ m^{-3}. In contrast, [58] reported N_2^+ densities, observed by the Dynamics Explorer satellite during the solar proton event of July, 1982, for polar latitudes, $n_0 \approx 1 \times 10^{10}$ m^{-3}, and mid-latitudes, $n_0 \approx 3 \times 10^9$ m^{-3}. We shall take these last densities as extreme values, because solar proton events are characterized by extreme ionospheric conditions.

The increase of ion density with latitude was also revealed in [53] under stormy geomagnetic conditions. Our assumption that number density is a function of alti-

tude only is clearly violated. However, [37] discussed evidence from neutral particle data that the density surplus at auroral latitudes propagates in a wave to the lower latitudes—this is time dependent behaviour we have not considered. Since we have adopted the observed property of bulk neutrality for our gas of ionized N_2, then we can expect the ion densities will also tend to toward uniformity in a similar fashion. This is supported by a theoretical study presented in [63], where local ionic enhancements of ten times the ambient value decay away in, at most, eleven hours during winter (the season in which our event occurred); but density depletions are far less stable, and are calculated to last no more than a few hours. Thus, it is the equatorial depletions that determine the time it takes for the ion density gradient with latitude to diminish.

The amount by which the N_2 density increases with temperature was found in [8] to double for an increase of 200 K in the thermospheric temperature. For the geomagnetic storm of February, 1974, [30] reported an increase of ten times over the density associated with typical conditions. It was also verified that all of the heavier neutral components—N_2 included—of the thermosphere were enhanced, regardless of latitude.

5.4 Conclusion

We have reviewed a sample of typical observations that bear directly upon our results for the number density n_0 of N_2^+ at 300 km and its thermospheric effective plasma temperature T. The conclusions dealing with T and n_0 that follow from our discussion can now be stated.

- T is probably overestimated, but not by much more than 300 K. The fact that two different methods yielded values of T which agree within their respective uncertainties and that other observations do not contradict our results are two reasons to be confident in the accuracy of our determination of T. The assumption of a uniform value of T for the thermosphere is a fair approximation at best, and under some extreme circumstances—such as the beginning of a storm—it is an entirely inappropriate assumption.

- We may have underestimated n_0, but not by more than an order of magnitude. We have accounted for the difference in the results obtained by two different methods: the difference being the extinction of 391.4 nm light by thermospheric N_2^+. Other observations do not discount our findings as unprecedented; in fact, they lie well within the realm of the physically possible. The assumption that n varies only with altitude suffers from the same problems as our isothermal conjecture.

The data analysis algorithm for primary scattering with extinction (PSE) can be deemed neither a complete success nor a dismal failure. It is a fact that, with a little coaxing, the algorithm did not collapse under the burden of poorly ordered data (due to a wobbling satellite) and, for a limited segment of data, was able to produce corrections to the observations and their ordering in time (hence altitude) such that an independent, but previously successful, method could produce similar results. This seems like enough evidence to propose that our prototype PSE algorithm is at least worthy of some attention. However, the overall accuracy is questionable, because of the unexpectedly large values of the corrections required by our best fit

model.

If our PSE analysis passed testing on better quality data, if such were extant or yet to be obtained, then it could be upgraded for general applications—it could be used to analyze other scattered or emitted wavelengths of other particles in order to test any assumed number density distribution. The scattered radiation need not have a natural source, but could be introduced as part of the experiment. Further extensions to include multiple and Rayleigh scattering would make sophisticated ground based observations possible, and that would allow for a detailed determination of the spatial structure of the scattering material.

Bibliography

[1] Anderson, D. E., and C. W. Hord. "Multidimensional Radiative Transfer: Application to Planetary Coronae." Planet. Space Sci., 25 (1977), 563–71.

[2] Anderson, D. E., et al. "Hydrogen Balmer Alpha Intensity Distributions and Line Profiles from Multiple Scattering Theory Using Realistic Geocoronal Models." J. Geophys. Res., 92 (1987), 7619–42.

[3] Anger, C. D., et al. "The Isis 2 Scanning Auroral Photometer." Appl. Opt., 12 (1973), 1753–67.

[4] Anger, C. D., and A. T. Y. Lui. "A Global View at the Polar Region on 18 December 1971." Planet. Space Sci., 21 (1973), 873–78.

[5] Arfken, G. Mathematical Methods for Physicists. 3rd rev. ed. Orlando: Academic Press, 1985.

[6] Bevington, P. R. Data Reduction and Error Analysis for the Physical Sciences. New York: McGraw-Hill, 1969.

[7] Bingel, W. A. Theory of Molecular Spectra. Germany: John Wiley, 1970.

[8] Blum, P. W. , C. Wulf-Mathies, and H. Trinks. "Interpretation of Local Thermospheric Disturbances of Composition Observed by ESRO 4 in the Polar Region." J. Geophys. Res., 15 (1975), 209–14.

[9] Brace, L.H. "F-Region Electron Temperature Signatures of the Plasmapause Based on Dynamics Explorer 1 and 2." J. Geophys. Res., 93 (1988), 1896–1908.

[10] Brace, L.H., N.W. Spencer, and G.R. Carignan. "Ionosphereic Electron Temperature Measurements and Their Implications." J. Geophys. Res., 68 (1963), 5397–5412.

[11] Brace, L.H., et al. "Deformation of the Night Side Plasmasphere and Ionosphere During the August 1972 Geomagnetic Storm." J. Geophys. Res., 79 (1974), 5211–18.

[12] Broadfoot, A. L. "Resonance Scattering by N_2^+." Planet. Space Sci., 15 (1967), 1801–15.

[13] Broadfoot, A. L. "Scattering of Twilight N_2^+ Emission." Planet. Space Sci., 16 (1968), 693–99.

[14] Broadfoot, A. L., and D. M. Hunten. "N_2^+ Emission in the Twilight." Planet. Space Sci., 14 (1966), 1303–19.

[15] Burrows, J. R., L. L. Cogger, and H. G. James, eds. Coordinated Ionospheric and Magnetospheric Observations from the ISIS 2 Satellite by the ISIS 2 Experimenters, No. 4. Greenbelt, Maryland: National Space Science Data Center, 1981.

[16] Chamberlain, J. W., and C. Sagan. "The Origin of Nitrogen Ionization in the Upper Atmosphere." Planet. Space Sci., 2 (1960), 157-64.

[17] Chamberlain, J. W., and D. M. Hunten. Theory of Planetary Atmospheres. London: Academic Press, 1987.

[18] Chandler, M. O., et al. "Model Calculations of Minor Ion Populations in the Plasmasphere." J. Geophys. Res., 92 (1987), 5885–95.

[19] Chandra, S., and J.R. Herman. "F-Region Ionization and Heating During Magnetic Storms." Planet. Space Sci., 17 (1969), 841–51.

[20] Cormack, A. M. "Representation of a Function by its Line Integrals, with Some Radiological Applications." J. Appl. Phys., 34 (1963), 2722–27.

[21] Cormack, A. M. "Representation of a Function by its Line Integrals, with Some Radiological Applications II." J. Appl. Phys., 35 (1964), 2908–13.

[22] Coulson, K.L. "Characteristics of the Radiation Emerging from the Top of a Rayleigh Atmosphere." Planet. Space Sci., 1 (1959), 277–84.

[23] Evans, J.V. "Midlattitude F-Region Densities and Temperatures at Sunspot Minimum." Planet. Space Sci., 15 (1967), 1387–1405.

[24] Feldman, P.D. "Daytime Ion Chemistry of N_2^+." J. Geophys. Res., 78 (1973), 2010–16.

[25] Grochulska, J. "Diffusion Equations for the Major Ions in the Mid-Lattitude Ionosphere and Plasmasphere." J. Atmos. Terr. Phys., 47 (1985), 423–39.

[26] Gorenflo, R., and S. Vessella. Abel Integral Equations: Analysis and Applications. A. Dold, B. Eckmann and F. Takens, eds. Lecture Notes in Mathematics, No. 1461. Berlin: Springer-Verlag, 1991.

[27] Hays, P. B., and R. G. Roble. "Atmospheric Properties from the Inversion of Planetary Occultation Data." Planet. Space Sci., 16 (1968), 1197–218.

[28] Hedin, A. E. "A Revised Thermospheric Model Based on Mass Spectrometer and Incoherent Scatter Data: MSIS-83." J. Geophys. Res., 88 (1983), 10170–88.

[29] Hedin, A. E. "MSIS-83 Thermospheric Model." J. Geophys. Res., 92 (1987), 4649–62.

[30] Hedin, A. E., et al. "Observations of Neutral Composition and Related Ionospheric Variatons During a Magnetic Storm in February 1974." J. Geophys. Res., 82 (1977), 3183–89.

[31] Hedin, A. E., et al. "Global Empirical Model of the Venus Thermosphere." J. Geophys. Res., 88 (1983), 73–83.

[32] Hernandez, G., and R. G. Roble. "Nighttime Variation of Thrmospheric Winds and Temperatures Over Fritz Peak Observatory During the Geomagnetic Storm of March 2, 1983." J. Geophys. Res., 89 (1984), 9049–56.

[33] Hoffman, J.H., et al. "Initial Ion Composition Results from ISIS 2 Satellite." J. Geophys. Res., 79 (1974), 4246–51.

[34] Huang, K. Statistical Mechanics. 2nd rev. ed. New York: John Wiley, 1967.

[35] Hunten, D. M. "Spectroscopic Studies of the Twilight Airglow." Space Sci. Rev., 6 (1967), 493–573.

[36] Ismail, S. Polar Cap Optical Emissions, M.Sc. Thesis, The University of Calgary, 1976.

[37] Jacchia, L. G., J. W. Slowey, and U. von Zahn. "Lattitudinal Changes of Composition in the Disturbed Thermosphere from ESRO 4 Measurements." J. Geophys. Res., 81 (1976), 36–42.

[38] Jackson, J. D. Classical Electrodynamics. 2nd rev. ed. New York: John Wiley, 1975.

[39] Johnson, F. S. "The Ion Distribution Above the F_2 Maximum." J. Geophys. Res., 65 (1960), 577–84.

[40] Jones, A. Vallance. Aurora. Holland: D. Reidel Publishing, 1974.

[41] Kittel, C., and H. Kroemer. Thermal Physics. New York: W. H. Freeman and Co, 1980.

[42] Lancaster, P., and M. Tismenetsky. The Theory of Matrices: with Applications. Orlando: Academic Press, 1985.

[43] Lenoble, J., ed. Radiative Transfer in Scattering and Absorbing Atmospheres: Standard Computational Procedures. Hampton, Virginia: A. Deepak Publishing, 1985.

[44] Liboff, R. L. Introductory Quantum Mechanics. Oakland: Holden-Day, 1980.

[45] Lorrain, P., D. R. Corson, and F. Lorrain. Electromagnetic Fields and Waves. New York: W. H. Freeman, 1987.

[46] Lui, A. T. Y. Initial Analysis of Data from the ISIS 2 Scanning Auroral Photometer, M.Sc. thesis, The University of Calgary, 1971.

[47] Mange, P. "The Distribution of Minor Ions in Electrostatic Equilibrium in the High Atmophere." J. Geophys. Res., 65 (1960), 3833–34.

[48] Mayr, H.G., and H. Volland. "Magnetic Storm Characteristics of the Thermosphere." J. Geophys. Res., 78 (1973), 2251–64.

[49] Meyer, S. L. Data Analysis for Scientists and Engineers. New York: John Wiley, 1975.

[50] Nagy, A.F. "Direct Measurements Bearing on the Extent of Thermal Non-Equilibrium in the Ionosphere." J. Geophys. Res., 68 (1963), 6401–12.

[51] Powers, D. L. Boundary Value Problems. 3rd rev. ed. San Diego: Harcourt Brace Jonavich, 1987.

[52] Press, W. H., et al. Numerical Recipes in C: The Art of Scientific Computing. Cambridge: Cambridge University Press, 1988.

[53] Prölss, G. W. "Magnetic Storm Associated Perturbations of the Upper Atmosphere: Recent Results Obtained by Satellite-Borne Gas Analyzers." Rev. Geophys. Space Phys., 18 (1980), 183–202.

[54] Rasmussen, C.E., et al. "Comparisons of Simultaneous Chatanika and Millstone Hill Temperature Measurements With Ionospheric Model Predictions." J. Geophys. Res., 93 (1988), 1922–32.

[55] Rees, M. H. Physics and Chemistry of the Upper Atmosphere. Cambridge: Cambridge University Press, 1988.

[56] Richards, P.G., et al. "The Behavior of the Electron Density and Temperature at Millstone Hill During the Equinox Transition Study September 1984." J. Geophys. Res., 94 (1989), 16969–75.

[57] Roble, R. G., and P. B. Hays. "A Technique for Recovering the Vertical Number Density Profile of Atmospheric Gases from Planetary Occultation Data." Planet. Space Sci., 20 (1972), 1727–44.

[58] Roble, R.G., et al. "Joule Heating in the Mesosphere and Thermosphere During the July 13, 1982, Solar Proton Event." J. Geophys. Res., 92 (1987), 6083–90.

[59] Roble, R.G., E.C. Ridley, and R.E.Dickensen. "On the Global Mean Structure of the Thermosphere." J. Geophys. Res., 92 (1987), 8745–58.

[60] St.-Maurice, J.-P., and R. W. Schunk. "Diffusion and Heat Flow Equations for the Mid-Lattitude Topside Ionosphere." Planet. Space Sci., 25 (1987), 907–20.

[61] Schunk, R., and J. C. G. Walker. "Thermal Diffusion in the Topside Ionosphere for Mixtures Which Include Multiply Charged Ions." Planet. Space Sci., 17 (1969), 853–68.

[62] Schunk, R.W., and A.F. Nagy. "Electron Temperature in the F-Region of the Ionosphere: Theory and Observations." Rev. Geophys. Space Phys., 16 (1978), 355–99.

[63] Schunk, R.W., and J.J. Sojka. "A Theorectical Study of the Lifetime and Transport of Large Ionospheric Density Structures." J. Geophys. Res., 92 (1987), 12343–51.

[64] Sharp, W.E. "Twilight Airglow 2. N_2^+ Emission at 3914 Å." J. Geophys. Res., 79 (1974), 1569–71.

[65] Solomon, S. C., P. B. Hays, and V. J. Abreu. "Tomographic Inversion of Satellite Photometry." App. Opt., 23 (1984), 3409–14.

[66] Solomon, S. C., P. B. Hays, and V. J. Abreu. "Tomographic Inversion of Satellite Photometry II." App. Opt., 24 (1985), 4134–45.

[67] Struve, W. S. Fundamentals of Molecular Spectrocopy. New York: John Wiley and Sons, 1989.

[68] Tepley, C. A. "Spectrophotometric Measurement Techniques of Weak Emissions in Twilight Airglow", World Ionosphere/Thermosphere Study, 2 (1989), 224-37.

[69] Thorne, A. P. Spectrophysics. London: Chapmann and Hall, 1974.

[70] Torr, D. G., et al. "An Experimental and Theoretical Study of the Mean Diurnal Variation of O^+, NO^+, O_2^+ and N_2^+ Ions in the Mid-lattitude F_1 Layer of the Ionosphere." J. Geophys. Res., 84 (1979), 3360–72.

[71] Walker, J. C. G. "Analytic Representation of Upper Atmospheric Densities Based on Jacchia's Static Diffusion Models." J. Atmos. Sci., 22 (1965), 462–63.

[72] Wallace, L., and M.B. McElroy. "The Visual Dayglow." Planet. Space Sci., 14 (1966), 677–708.

[73] Wiens, R. H., and L. L. Cogger. "Observation of Winter Enhancement of Twilight λ3914 by ISIS 2." J. Geophys. Res., 80 (1975), 4351–58.

[74] Witten, R. C., and I. G. Poppoff. <u>Fundamentals of Aeronomy</u>. New York: John Wiley , 1971.

[75] Zipr, E.C., and W.G. Fastie. "An Observation of the (0,0) Negative Band of N_2^+ in the Dayglow." <u>J. Geophys. Res.</u>, 69 (1964), 2357–67.